

Chapter 4

Highly self-organized growth of Carbon Nitride

§ 4.1. Introduction to Carbon Nitride

The prediction in 1989 by Liu and Cohen [1] of super-hard β -C₃N₄ sparked extensive worldwide research into this new material. The prediction arose from the empirical formula proposed in the same paper:

$$B = \frac{1971 - 220\lambda}{d^{3.5}} \quad (4.1)$$

where B is bulk modulus (Mbar), λ is the ionicity and d the bond length (Å).

Using the empirical formula, clearly, to achieve high bulk modulus (B) the elements involved in bonding must have low ionicity (λ) and short bond length (d). This indicates the light elements in the periodic table (B, C, N, and Si) may have favourable properties to produce a super-hard compound. Hence BN_x and CN_x were identified [1] and developed as possible candidates to have a bulk modulus similar to or larger than diamond.

Liu and Cohen [1] predicted β -C₃N₄ based on the known β -Si₃N₄ structure, with C substituted for Si (see Figure 4.1(a)). This will clearly have low ionicity (~7%) and also a short equilibrium volume bond length (~1.47 Å), therefore a high bulk modulus is expected. Using first principle pseudopotential calculations, a cohesive energy of 81 eV per cell and bulk modulus of 4.27 (±0.15) Mbar were calculated [1]. This relatively large cohesive energy suggested that β -C₃N₄ will be at least metastable. The structure was further predicted to have a wide band-gap and

high thermal conductivity and hence may have potential applications as electron emitters, variable bandgap semiconductors and as transparent hard coatings [2]. But it was the prediction that β - C_3N_4 would be harder than diamond that caught researchers' imagination and made it the subject of many studies to try to make thin films or bulk quantities of this material.

§ 4.1.1. Structures and properties of C_3N_4 phases

Since the theoretical study by Liu and Cohen [1] was published, further significant assumptions were made based on state-of-the-art first principle calculations (such as local density approximation (LDA)). Different structural forms of C_3N_4 have been predicted [3,4,5,6] including α - C_3N_4 , β - C_3N_4 , graphitic- C_3N_4 (g- C_3N_4), pseudocubic- C_3N_4 (bl- C_3N_4) and cubic- C_3N_4 , as shown in Figure 4.1.

The β - C_3N_4 structure consists of buckled layers stacked in an AAA sequence (as seen in Figure 4.1(a)). The unit cell is hexagonal $P6_3/m$ space group and contains two formula units (14 atoms) with local order such that C atoms occupy slightly distorted tetrahedral sites while N atoms sit in nearly planar triply-coordinated sites [1]. The structure can be further considered as a complex network of three, four and sixfold CN_4 tetrahedra that are linked at the corners [1]. The atomic coordination suggests sp^3 -hybridised C bonded to sp^2 -coordinated N.

In contrast, the α - C_3N_4 structure [3] (Figure 4.1(b)) can be described as an ABAB stacking sequence, in which A is the β - C_3N_4 unit cell and B its mirror image. The unit cell contains 28 atoms and has $P3_1c$ symmetry. Graphitic- C_3N_4 (Figure 4.1(c)) can also be viewed as an ABAB stacking sequence but of the planar structure [7]. The unit cell contains 14 atoms and exhibits $P\bar{6}m2$ symmetry. Another predicted structure is the pseudocubic α - $CdIn_2Se_4$ structure (Figure 4.1(d)), which is classified as a 'defective-zincblende' structure [8]. It exhibits $P\bar{4}2m$ symmetry and contains seven atoms in the unit cell. Finally, the cubic- C_3N_4 structure (Figure 4.1(e)) is based on the high pressure Willemite-II structure [9], where C is substituted for Zn and Si and N are substituted for O. It was found that this structure adopts cubic $I\bar{4}3m$ symmetry and has 28 atoms in the unit when the structure is allowed to relax.

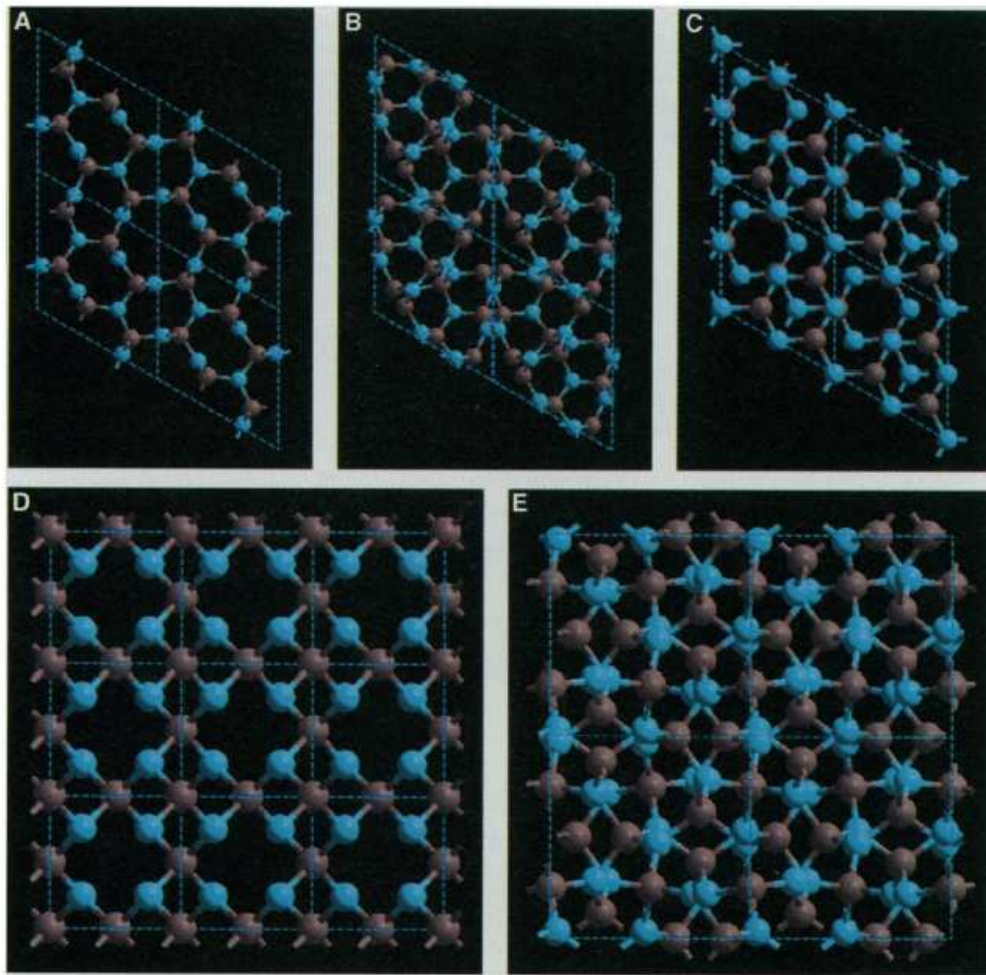


Figure 4.1 Representation of the (a) β -C₃N₄, (b) α -C₃N₄, (c) g-C₃N₄, (d) pseudocubic-C₃N₄, (bl-C₃N₄) and (e) cubic-C₃N₄ structures down the [001] axis. The carbon and nitrogen are depicted as grey and blue spheres, respectively [3].

Theoretical pseudopotential plane-wave (PP) calculations by Teter *et al.* [3] and other groups [10,11] have been used to calculate the stability and properties of the C₃N₄ phases. Table 4.1 shows that α -C₃N₄ and g-C₃N₄ are theoretically predicted to be the most energetically stable phases (lowest E_0), then β -C₃N₄, with cubic- and pseudocubic-C₃N₄ being significantly higher in energy.

Table 4.1 Structural energy (E_0) and bulk modulus (K_0) of predicted C_3N_4 phases [3]. The order of magnitude of E_0 was also confirmed by full-potential linearised augmented plane-wave (FP-LAPW) and the order of magnitude of K_0 was also confirmed by Linear Muffin-Tin Orbitals (LMTO), Augmented Spherical Wave (ASW) and FP-LAPW [11]. The value for K_0 for g- C_3N_4 was taken from [8].

	α - C_3N_4	β - C_3N_4	g- C_3N_4	bl- C_3N_4	cubic- C_3N_4
E_0 (eV/unit)	-1598.669	-1598.403	-1598.710	-1597.225	-1597.388
K_0 (GPa)	425	451	51 [8]	448	496

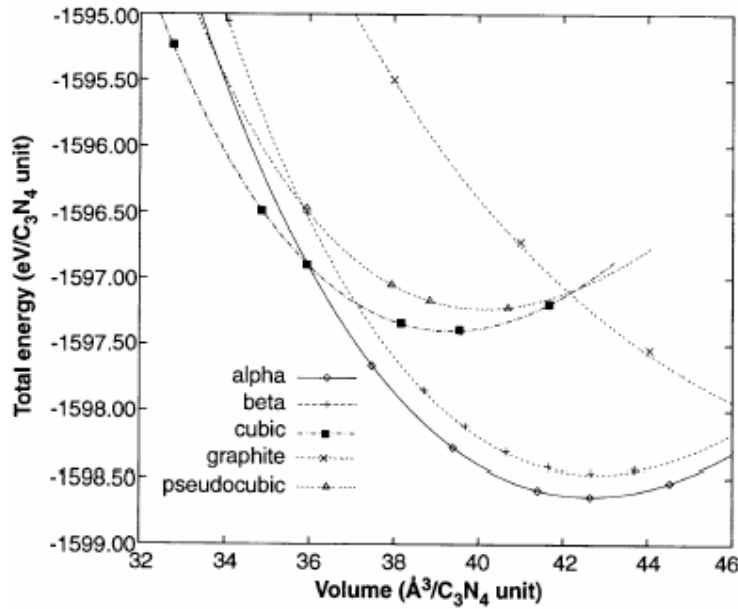


Figure 4.2 Total energies as a function of volume for different C_3N_4 phases. Curves were generated from fits to the calculated data points using the Birch equation of state [3].

The transition pressure from α - to cubic- C_3N_4 and g- to cubic- C_3N_4 is predicted to be 68 and 12 GPa, respectively, as cubic- C_3N_4 becomes more energetically stable as volume is decreased [3] (Figure 4.2). This is significant as cubic- C_3N_4 is predicted to have the highest bulk modulus (K_0) of all the phases (Table 4.1) and

hence could be achieved via a high pressure synthesis route *e.g.* LP-PLA. In fact a K_0 of 496 GPa (PP) [3] for cubic- C_3N_4 is calculated, which is significantly higher than that of diamond, obtained experimentally as 442 GPa. It must be noted that the predicted K_0 value will depend on the theoretical approach [11], however, all phases (except g- C_3N_4) and approaches have shown K_0 to be comparable to or higher than that of diamond.

§ 4.1.2. Bonding in C_3N_4

The bonding in C_3N_4 is important for characterisation and identification of the material. The material will have carbon four-coordinated with nitrogen (sp^3 hybridised, except the graphitic phase) and nitrogen three-coordinated with carbon (sp^2 or sp^3 hybridised depending on whether it is planar (lone pair in one of $2p$ orbitals) or pyramidal in geometry, respectively).

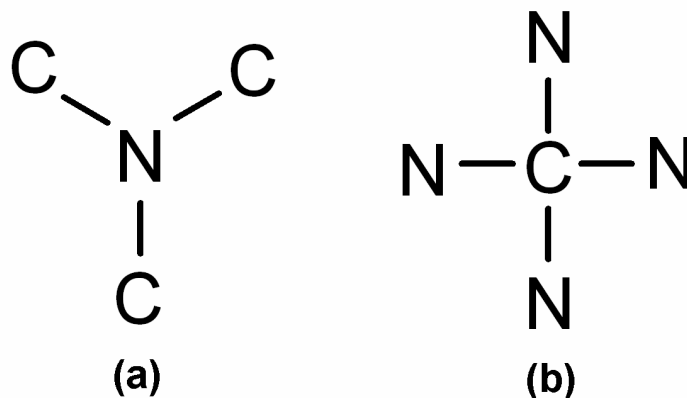


Figure 4.3 Chemical bonding in C_3N_4 .

Liu and Cohen [1] predicted β - C_3N_4 via a derivation of the β - Si_3N_4 structure, and hence as β - Si_3N_4 has sp^2 planar nitrogen this was assumed for β - C_3N_4 also. However, it was later predicted that a combination of sp^2 and sp^3 geometry will be present [3,8,11,12]. The nitrogens in the β - C_3N_4 structure which are attached to

three 12-membered C-N₁ rings are likely to be dominant in sp^2 character, whereas those present in smaller six- and eight-membered C-N rings, will have some sp^2 , but overall be dominant in sp^3 character due to the smaller size of these rings [12].

In α -C₃N₄, since all the N sites are attached to 6-membered C-N rings only, almost all will be sp^3 rather than sp^2 hybridised [12]. This actually gives α -C₃N₄ a unique feature of a negative Poisson ratio in all dimensions [13], which allows the C-N-C bond angles to approach planarity under tension.

In the graphitic-C₃N₄ planar structure, bonding consists of a 3-coordinated C which is sp^2 hybridised to two 2-coordinated nitrogens (denoted as 'N₂'), in a 1,3,5-triazine ring, and a nitrogen in a planar sp^2 configuration (denoted as 'N₁' site), connecting these rings [14] (Figure 4.4). Non-planar geometry is similar but has three 6-membered rings attached to the C-N rings, this provides sp^3 rather than sp^2 hybridised bonding and results in buckling of the graphitic sheets [15]. However, the planar g-C₃N₄ structure is more common and in referral to g-C₃N₄ the planar structure is assumed.

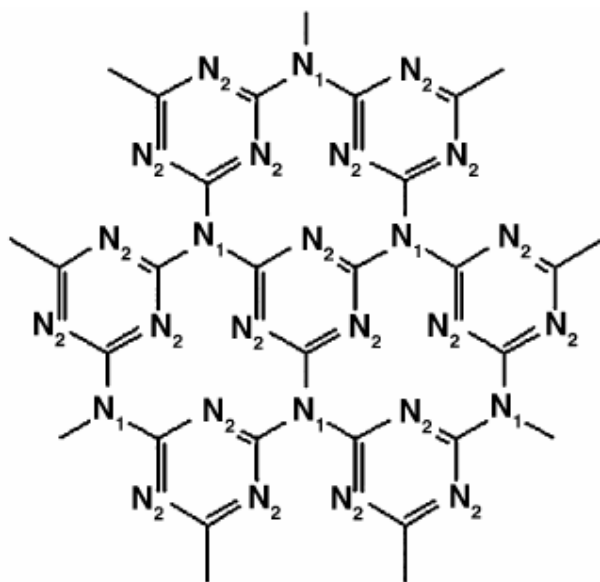


Figure 4.4 Structure of planar g-C₃N₄ [14]. Nitrogens occupy two different positions in the layer, labelled N₁ and N₂.

The other phases will not be considered as they have previously been shown to be energetically unfavourable. Hence, during characterisation, the presence of C_3N_4 should show sp^3 C-N bonding, except for the g- C_3N_4 phase which will show sp^2 C-N bonding. Furthermore, C will have sp^3 geometry only, and N will have sp^2 or sp^3 geometry, with sp^2 more prominent in β - than α - C_3N_4 . However, it must be noted that these predictions arise from theoretical calculations, and some debate still surrounds the exact nature of the bonding. In particular, the ratios of sp^2 to sp^3 are unsubstantiated, which would otherwise allow conclusive identification of a particular C_3N_4 phase (with an appropriate technique).

§ 4.1.3. Previous C_3N_4 Research

Research into the production of C_3N_4 has occurred via various techniques including: hot filament chemical vapour deposition (HFCVD) [16,17,18]; plasma-enhanced chemical-vapour deposition (PECVD) [10,11, 19, 20]; reactive radio frequency sputtering [21,22]; dc magnetron sputtering [23,24,25]; ion beam assisted sputtering [26,27,28,29]; laser ablation [30,31]; chemical synthesis [14,32,33]; mechano-chemical synthesis [34]; filtered cathodic vacuum arc [35] and reactive ion implantation [36,37]. However, in the majority of cases only amorphous carbon nitride thin films have been produced (although this has been shown to have interesting properties [38]), or material which has a low nitrogen content.

Crystalline carbon nitride synthesis has been claimed by a number of authors, especially for the β - C_3N_4 phase (see reviews [12,39]). However, to date, no satisfactory evidence has been presented that a crystalline solid of the proposed kind has been synthesised [39,40,41]. The critical review by Matsumoto *et al.* [39] reported that crystalline diffraction patterns could be indexed to other carbon phases. Furthermore, other analysis techniques are subject to interpretation, with differences in, for example, sp^2 and sp^3 -bonded nitrogen or carbon that are hard to analyse conclusively. Nevertheless, many studies have still claimed the existence of C_3N_4 via comparisons of experimental and theoretical d -spacings from diffraction patterns and evidence of N-C sp^3 bonding. It is still believed that the formation of a

metastable crystalline carbon nitride solid is possible when an appropriate precursor [42,43,44,45,46] is used via a chemical route [47,48,49] using a catalyst, under highly non-equilibrium deposition conditions [50] or under higher pressure [51,52,53,54].

Various techniques have been used to prove the synthesis of C_3N_4 , such as: selected area electron diffraction (SAED) patterns; powder X-ray diffraction (XRD) patterns, high-resolution transmission electron microscopy (HRTEM); X-ray photoelectron spectroscopy (XPS); UV-Visible absorption spectroscopy; Raman spectroscopy; Fourier transform infrared (FTIR) spectroscopy; Nuclear magnetic resonance (NMR) spectroscopy; Electron loss spectroscopy (EELS) and near-edge X-ray absorbance (NEXAFS) spectroscopy.

Techniques have been critically evaluated, with papers claiming that EELS [55] and NEXARS [56] can conclusively distinguish between sp^2 and sp^3 hybridised carbon, whereas it has been suggested [57] that FTIR cannot be taken to distinguish between those bonding states in carbon nitride. NMR also is widely reported to be able to characterise conclusively the hybridisation of C, via chemical shifts. Use of XPS has been reported to be difficult in distinguishing sp^2 and sp^3 geometry N, but is extensively used to identify sp^3 C-N bonding and hence to indicate C_3N_4 . Furthermore, SAED is said to be able to show the existence of polycrystalline and crystalline C_3N_4 but that occurrences of carbon phases and allotropes, graphite, chaolite, *etc.* [58,59,60,61] must be excluded. Powder XRD is more commonly used, but sometimes very noisy and few or obscure XRD patterns [62,63,64,65] make conclusive proof of synthesis difficult. When the elemental compositions were given, XPS, EELS and Energy Dispersive X-ray analysis (EDX) were mostly used. However, XPS depends on sensitivity factors, the obtained N/C ratios are only estimates rather than their true contents. Although EELS is very sensitive to the hybridisation of light elements [66], uncertainties can arise due to a overlap between crystalline/amorphous regions in some CN_x materials [67]. Also EDX is, in principle, not sensitive enough to provide the exact composition of light elements, such as carbon and nitrogen. Therefore, it is clear that analysis is not straightforward, and the use of complementary and commercially available analysis techniques is needed in order to identify C_3N_4 satisfactorily. Also, the exclusion of all the carbon phases

within synthesised CN_x materials is inevitable in order to prove the synthesis of crystalline carbon nitride.

§ 4.1.4. Aim of this study

The main aim of the project was to synthesise CN_x nanostructures using the previously unreported technique (for these materials) of liquid phase- pulsed laser ablation (LP-PLA). The hope was to produce crystalline C_3N_4 which we might expect to be in the α -, β - or graphitic- phase, as these are the most energetically favourable.

Since the formation of diamond and other hard carbon materials is achieved under pressure or shock compression from graphite and fullerene [68,69,70], it is reasonable to expect that LP-PLA may be a suitable synthesis technique for C_3N_4 due to the extreme conditions it creates, namely, high temperature, high pressure and high density (see chapter 2 for details). Additionally, the use of a nanosecond laser and quenching by the liquid phase will result in a non-equilibrium process. These unique conditions may therefore produce crystalline C_3N_4 provided there are suitable C-N containing precursors with high nitrogen content. Furthermore, the nature of LP-PLA synthesis conditions may result in the formation of free-standing C_3N_4 phases (*i.e.* nanoparticles (NPs), nanorods (NRs) or other shapes) that have previously been unreported, as compared with mainly C_3N_4 films had been claimed in the past [71,72].

In this chapter, more recent progress in the synthesis of unique, highly ordered nanostructures of crystalline carbon nitride is discussed via laser ablation of a graphite target submerged in aqueous ammonia solution. In attempting to produce C/N materials, the LP-PLA parameters were varied (see chapter 3 for experimental details). These included parameters such as the target material, liquid phase material, wavelength, pulse duration and laser setup, *e.g.* distance from lens to target. Once these were decided, other parameters, such as laser fluence, ablation time and the concentration of ammonia solution were varied, and the project involved studies into how these affected the products. It was shown that for C_3N_4 , a Group IV-V covalent compound, a range of self-assembled arrays of NPs, NRs, nanoleaf, and mesoflowers

can be produced, and this also suggested that the route described here can be applicable to the synthesis of nanostructures of other similar materials.

§ 4.2 General nanostructural features in solid-liquid growth

Details of the processing of carbon nitride nanocrystals by LP-PLA can be found in Chapter 3.1. After ablation, a pale colour colloidal suspension was obtained depending on the synthesis conditions, which contained a mixture of unreacted target materials and ablation product, both in the form of NPs, remaining in the cell. Figure 4.5 shows how the as-prepared suspension changed from colourless (0 h), to pale brown (3 h), and then dark brown (7 h), dependent on the ablation time, indicating an increase in solid product and/or a change in composition of the solid due to prolonged interaction with the laser. The suspension was stable, with no precipitate being observed for months or even longer.

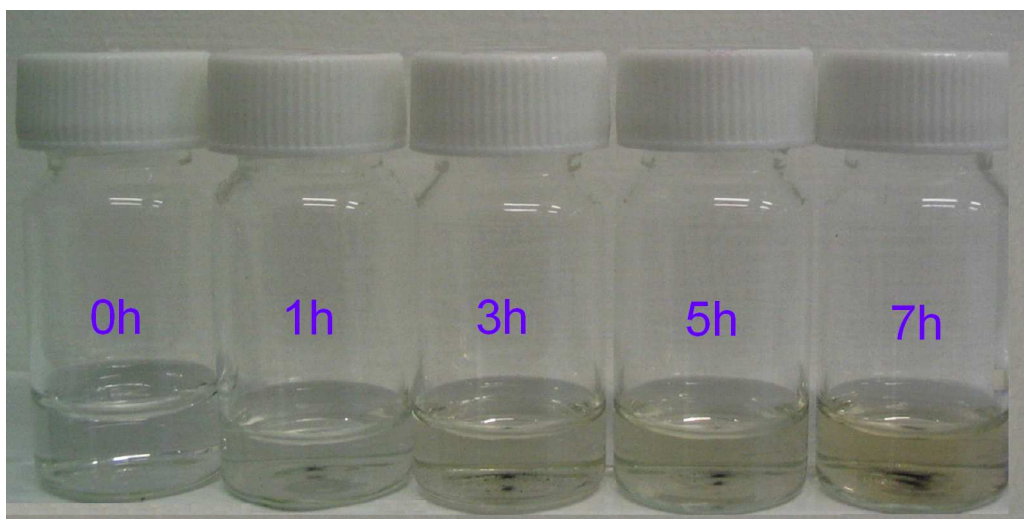


Figure 4.5 Photograph of the colour changes of the as-prepared suspensions after ablation for different times (35% ammonia solution, laser fluence 100 mJ per shot).

§ 4.2.1 Identification of a carbon nitride phase

Elemental analysis of the prepared ablation product gave the percentage composition by weight as: C 38.56, N 50.08, O 9.31, H 2.05 (wt%). This indicated that the average composition was $C_3N_{3.35}O_{0.54}H_{1.9}$, in comparison with the theoretical C_3N_4 empirical stoichiometry [2,3]. The presence of oxygen can be partly explained due to the prolonged exposure of the samples to the laboratory atmosphere leading to possible contamination by absorbed or adsorbed water vapour. Alternatively, the oxygen may be present as a result of reaction between the graphite surface and water (or OH radicals) as a result of the high temperatures in the plume.

The single broad peak in the X-ray diffraction pattern (Figure 4.6(a)) near 25.8° corresponds to an interlayer d -spacing of 3.42 \AA , which is similar to the d -spacing reported for carbon nitride spheres [73,74], and in good agreement with the calculated values for α - C_3N_4 and β - C_3N_4 in the hexagonal lattice reported in refs. [75,76].

TEM images (Figure 4.6(b)) showed that highly uniform spheroid-shaped NPs were produced after 30 min laser ablation at low laser power (50 mJ). The size distribution was obtained by measuring the diameters of more than 800 particles in sight on the given micrograph (Figure 4.6(b)), and this gave an average diameter for the NPs of ~ 8 -12 nm (see Figure 4.6(c)). An SAED pattern (Figure 4.6(d)) recorded from particles without any tilt indicated that the NPs were polycrystalline. The first four peaks from the centre, with interlayer d -spacings of 2.45, 2.15, 1.52 and 1.31 \AA , respectively, were indexed as (201), (102), (103) and (222) with reference to the calculated structure for α - C_3N_4 [3,76]. Table 4.1 also shows a good comparison between calculated d -spacings and theoretical d -spacing for α - C_3N_4 . The calculated intensities match theoretical intensities very well for Figure 4.6(d) and the percentage error is less than the experimental error. Overall, given the large number of planes that have been indexed this is strong evidence that α -phase carbon nitride may have been formed predominantly.

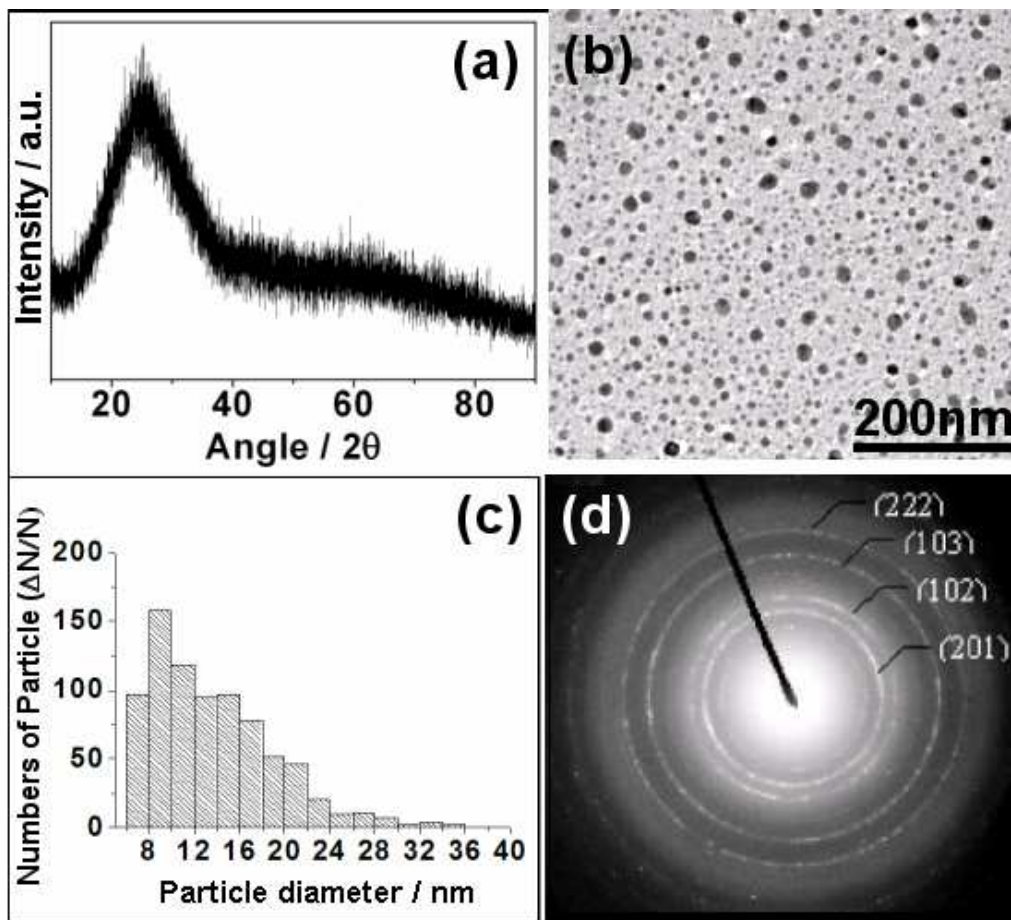


Figure 4.6 (a) A representative XRD pattern recorded using Cu $K\alpha$ ($\lambda = 0.154$ nm) radiation in the 2θ range of 10 to 90° with a 2θ step size of 0.005° and a step time of 4 s. (b) A TEM image of the NPs produced after 30 min ablation of a graphite target in 35% ammonia solution (50 mJ laser power). (c) Size distribution of the NPs by measuring the diameters of more than 800 particles. The average particle size is ~ 8 – 12 nm. (d) SAED pattern of the NPs, which corresponds closely to the calculated interlayer d -spacing of α - C_3N_4 .

Table 4.2 Calculated d -spacings for as-prepared NPs with comparison to theoretical α -C₃N₄ (% error between experimental and theoretical values shown). Experimental d -spacings were produced from Figure 4.6(d) using the computer program ‘Process diffraction’ [77], CaRIne 3.1 crystallography and the equations outlined in section Chapter 3.3.5.

Experimental		α -C ₃ N ₄ (Theoretical)			% Error
$d / \text{Å}$	Intensity	$d / \text{Å}$	(hkl)	Intensity	
2.45	Strong	2.40	201	Strong	-2.08
2.15	Medium	2.18	102	Medium	1.38
1.83	Strong	1.90	112	Strong	3.68
1.52	Weak	1.51	103	Very weak	-0.66
1.31	Strong	1.33	222	Medium	1.50
1.24	Very Weak	1.24	321	Medium	0.00
1.16	Medium	1.20	303	Medium	3.33
1.10	Medium	1.10	313	Weak	0.00
1.08	Weak	1.08	330	Weak	0.00
0.99	Very Weak	0.99	323	Weak	0.00
0.91	Very Weak	0.90	205	Very Weak	-1.11
0.81	Medium	0.80	433	Very Weak	-1.25

It was also found that the structural order of the carbon nitride increased for longer ablation time, leading to NR-like structures with a crystalline C₃N₄ tip. Figure 4.7(a) contains a representative TEM image of NRs from samples after 5 h laser ablation. Those NRs were very straight and smooth along the whole length, in a highly aligned arrangement. It revealed that the NRs have sharp tip-like ends. Figure 4.7(b) shows a SAED pattern from the [110] zone-axis indicating a single crystal of C₃N₄. Diffraction patterns taken from different parts of the NRs show

exactly the same pattern, which indicates the single crystallinity of the whole NR. Figure 4.7(c) shows a HRTEM micrograph of the (102) planes corresponding to α - C_3N_4 crystalline with an interplanar distance of 0.218 nm [76], which was recorded from the region at the top of the NR indicated by the open box in Figure 4.7(a).

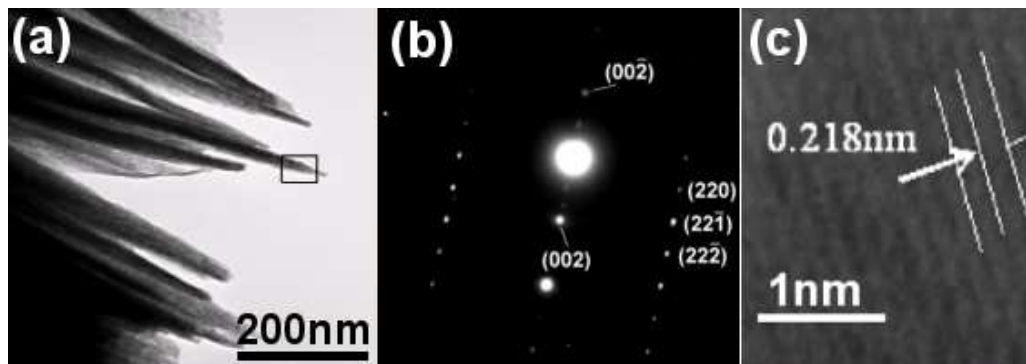


Figure 4.7 (a) TEM image of carbon nitride NRs synthesized using a solid-liquid laser ablation system for 5 h (50 mJ laser power). (b) SAED pattern of the tip of a NR from the [110] zone-axis indicating the area is single crystal C_3N_4 . (c) High-resolution TEM image of the region at the top of the NR indicated by the open box in (a).

Further information regarding the chemical bonding structure was obtained from FTIR spectroscopy. Figure 4.8 is an FTIR spectrum from the NRs (Figure 4.6(a)) prepared by 5 h of laser ablation, that clearly shows several peaks related to the chemical bonding between carbon and nitrogen [78]: the region 1000 - 1500 cm^{-1} corresponds to C-N single bonding, while the regions 1500 - 1750 cm^{-1} and 2150 - 2300 cm^{-1} are related to C=N and C \equiv N bonding, respectively. In our case, the two peaks at 1034 cm^{-1} and 1384 cm^{-1} correspond to the C-N stretching mode. The absorption bands at 1637 cm^{-1} are assigned to the stretching vibrational modes of the C=N. Moreover, a small but clear peak at 2264 cm^{-1} can probably be attributed to C \equiv N bonds, although it is much weaker compared with the other stretching modes. A broad band centred at 3434 cm^{-1} is due to NH group vibrations [79].

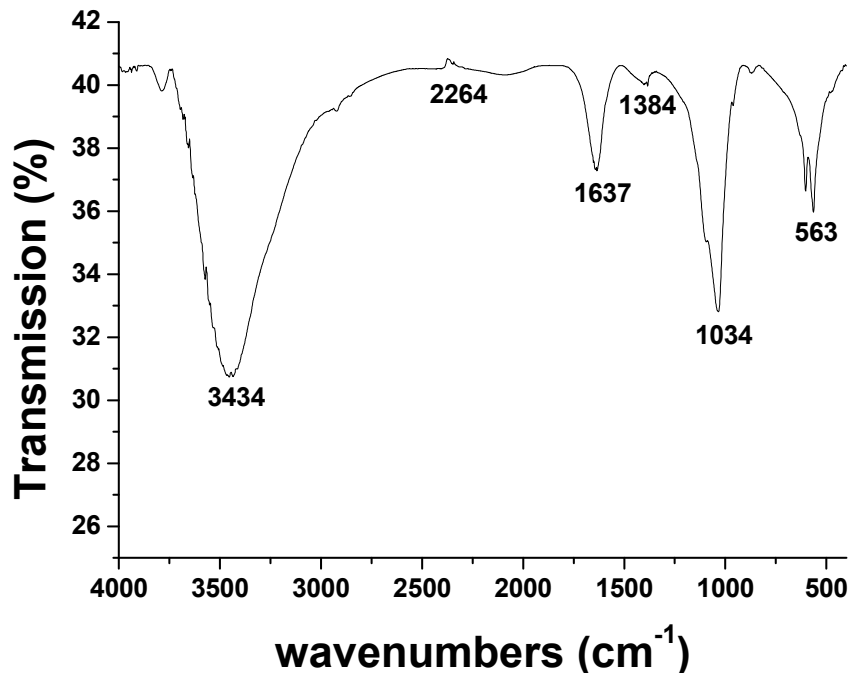


Figure 4.8 FTIR spectrum of the NRs showing two peaks at 1034 cm^{-1} and 1384 cm^{-1} corresponding to C-N stretching modes. The absorption bands around 1637 cm^{-1} and 2264 cm^{-1} are assigned to the vibrational modes of C=N and C≡N bonds, respectively, which suggests the formation of crystalline $\alpha\text{-C}_3\text{N}_4$.

The $\alpha\text{-C}_3\text{N}_4$ structure is predicted to have a lower energy and is more stable than all the other structures, at all volumes [1,3]. In fact, the existence of a metastable $\alpha\text{-C}_3\text{N}_4$ with a hexagonal structure ($a = 6.4665\text{ \AA}$, $c = 4.7097\text{ \AA}$, space group: $P3_1c$ (159)) has been confirmed by many researchers C_3N_4 [3,76]. The lattice indices of a_0 and c_0 in our experiment were calculated to be 6.6145 \AA and 4.7297 \AA from the spacing of the (201) and (103) planes, which are slightly larger than the values reported previously [3,76]. However, since $\alpha\text{-C}_3\text{N}_4$ and $\beta\text{-C}_3\text{N}_4$ have similar total energies, crystal structures, compositions, bulk moduli, bandgaps, and atomic densities, we believe that some of the $\beta\text{-C}_3\text{N}_4$ phase also exists in our system.

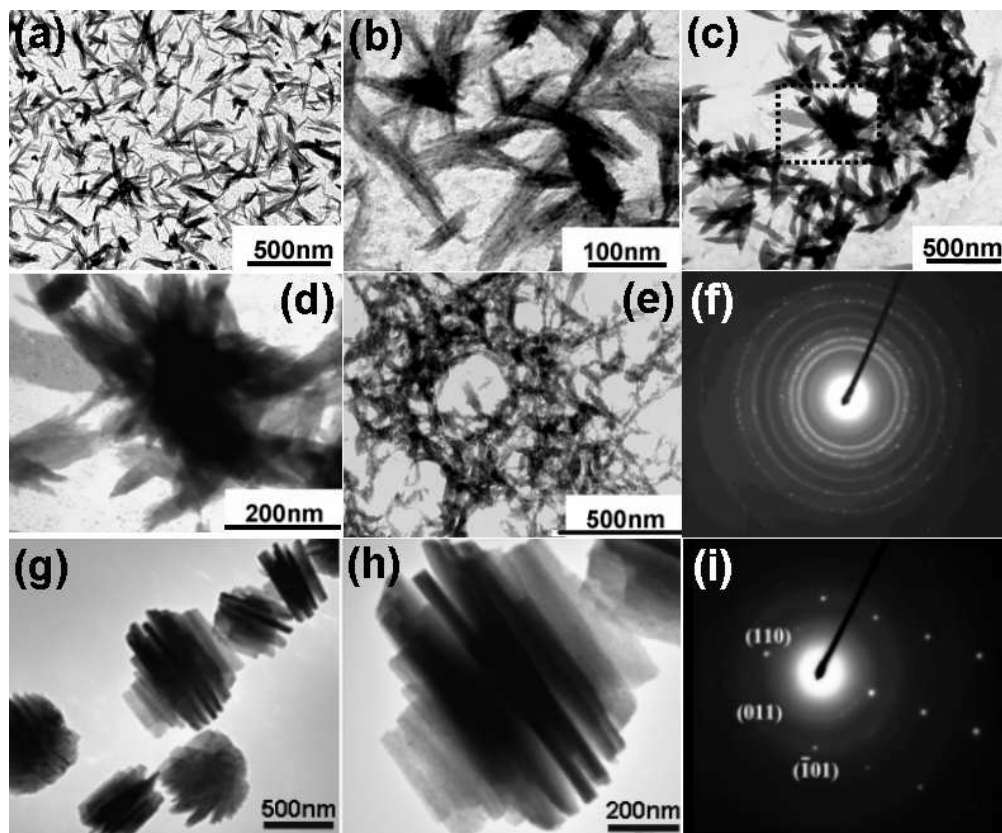


Figure 4.9 TEM images of samples produced by LP-PLA of a graphite target in 35% ammonia solution (laser fluence at 100 mJ per pulse) for durations of: (a) and (b) 1 h, (c) and (d) 3 h, (e) 5 h (laser power at 125 mJ), 2 h (g) and (h) (laser power at 50 mJ). (a) ‘Leaf-like’ structures are formed after only short ablation times. The higher magnification image of these, (b), shows that these structures are composed of smaller NRs. For longer ablation times, (c), the leaf-like structures increase in size and coalesce to form larger, denser, structures. The higher magnification image (d) of the region enclosed by the dashed lines shows that the surface of these structures is smooth. For even longer ablation times, (e), the denser structures begin to assemble together to form microscale networks. (f) A typical SAED pattern from the leaf-like nanostructures in (a), which corresponds closely to the calculated interlayer d -spacing of β - C_3N_4 . (g) NR aggregates with better developed layer surface after 2 h ablation at lower 50 mJ laser power. (h) Individual NRs from (g) that have aggregated. (i) SAED dot pattern of a NR from (h) indicating the area is single crystal and consistent with crystalline β - C_3N_4 .

Table 4.3 Calculated d -spacings for as-prepared nanoleaves with comparison to theoretical β -C₃N₄ (% error between experimental and theoretical values shown). Experimental d -spacings were produced from Figure 4.9(f) using the computer program ‘Process diffraction’ [77], CaRIne crystallography and the equations outlined in section Chapter 3.3.5.

Experimental		β -C ₃ N ₄ (Theoretical) [76]			% Error
$d / \text{Å}$	Intensity	$d / \text{Å}$	(hkl)	Intensity	
3.214	Strong	3.220	110	Strong	0.186
2.727	Strong	2.788	200	Strong	2.188
2.285	Medium	2.256	101	Medium	-1.285
1.924	Medium	1.958	111	Medium	1.736
1.627	Medium	1.610	220	Medium	-1.056
1.377	Medium	1.348	221	Medium	-2.151
1.320	Weak	1.310	311	Very Weak	-0.763
1.065	Weak	1.073	330	Weak	0.746
1.013	Very Weak	1.007	302	Weak	-0.596
0.939	Very Weak	0.960	421	Very Weak	2.188
0.888	Very Weak	0.888	322	Very Weak	0.000

Indeed, unusual β -phase carbon nitride nanostructures were observed during the TEM analysis depending upon the process conditions and especially upon the ablation time. These nanostructures were most likely formed as a result of the self-organising and close packing of the NPs as the suspension was dried out. Figure 4.9(a) and (b) show that after 1 h of ablation (laser fluence at 100 mJ per pulse), one-dimensional structures are formed of length \sim 200 nm and width 30-50 nm. Since both ends of the flat structures taper to a point, they resemble the shape of a leaf, and so henceforth have been termed ‘leaf-like’ structures. The high magnification image (Figure 4.9(b)) shows that these structures are themselves composed of a large number of smaller NRs that have packed together in an ordered arrangement to form

the leaf-like shapes. After ablation times of ~ 3 h (Figure 4.9(c) and (d)), the leaf-like structures coalesce to form larger, denser, structures with a smooth surface, which start to connect together. For ablation times around 5 h and laser power at 125 mJ (Figure 4.9(e)), these denser structures form a network of microscale structures.

Figure 4.9(f) shows a typical SAED ring pattern (obtained without any tilting) from the leaf-like nanostructures in Figure 4.9(a), which indicates that these structures are polycrystalline. Table 4.2 shows a very good comparison between calculated and theoretical $\beta\text{-C}_3\text{N}_4$ d -spacings from these nanostructures, with a maximum percentage error of 2.188. Furthermore, the experimental intensities matched closely those expected from theoretical calculations. The percentage difference also compares well with the experimental d -spacing error. Using equation 3.4 (Chapter 3.3.5), the error is $\sim 2\text{-}3\%$ and is almost entirely due to the inaccuracy in measuring the distance between rings from the patterns (which is hard to define). Hence, as the percentage error is less than the experimental error throughout, the indexing can be considered valid. These results are consistent with the SAED patterns and peaks previously assigned to single crystalline carbon nitride NRs [34]. At lower laser power (*e.g.* 50 mJ per pulse), NR aggregates appear with better developed layer surfaces after 2 h ablation. These are similar to the leaf-like nanostructures in that they are made up of NRs. However, in this case, the NRs are significantly wider and produce a very different shape. From Figure 4.9(h), the NR width is approximately 50 nm and is highly uniform throughout the structure. A well defined SAED dot pattern (Figure 4.9(i)) from the rod tips (Figure 4.9(h)) can be indexed, again using theoretical d -spacings, to $\beta\text{-C}_3\text{N}_4$ (preferential) of the [111] zone-axis. This indicates that the rods that make up the structure are a single crystal, and hence the NR aggregates are also made up of crystalline material. The SAED dot pattern could not be indexed to other phases or materials, so although this technique is not as reliable as ring patterns it nevertheless provides very strong evidence that $\beta\text{-C}_3\text{N}_4$ has been produced.

The XPS spectrum of most ablation products shows peaks for carbon and nitrogen as expected, but also for oxygen, other surface impurities and adsorbates. The C 1s peak (Figure 4.10(a)) has been deconvoluted into two peaks centred at 284.8 and 287.7 eV. The peak at 284.8 eV has been assigned previously as

‘graphitic carbon’, which includes contributions from graphite-like or amorphous carbon within the material along with adventitious carbon adsorbed on the surface, as well as C=C (284.6 eV), sp^3 C-C (284.7 eV) and C=N (284.8 eV) [27,72,80,81]. However, the peak at 287.7 eV has been assigned only to sp^3 -bonded C in C-N [82], with some workers [72,80,81] also assigning the highest deconvoluted peak to sp^3 C-N but at a slightly lower energy (~287.0 eV). The XPS study of CN_x films by Le Normand *et al.* [83] further states that the presence of sp^3 C-N is indicated by the presence of all peaks between 287.2-287.7 eV. Therefore, it can be concluded that sp^3 C-N bonds are present in the ablated product, which is consistent with C_3N_4 .

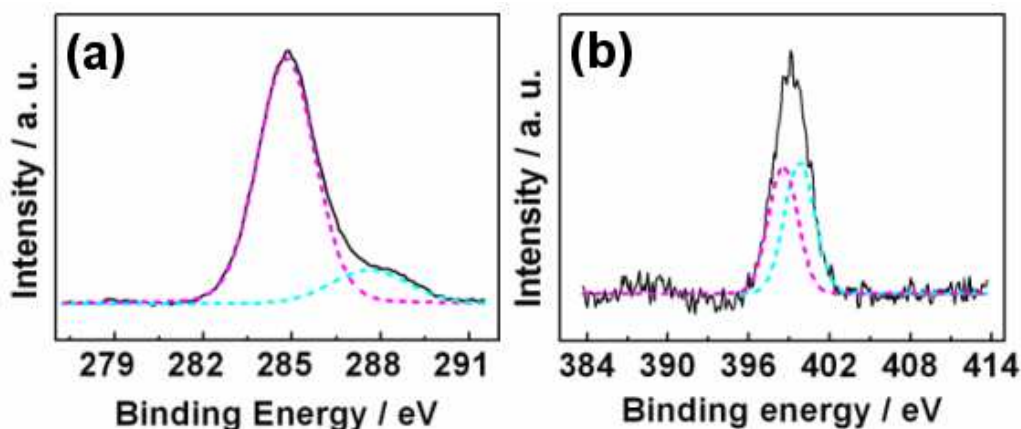


Figure 4.10 (a) C 1s and (b) N 1s XPS spectra of the product obtained from LP-PLA after 5 h ablation (125 mJ laser power). After background subtraction, the spectra were deconvoluted into 2 Gaussian line-shaped peaks centred at 284.8 and 287.7 eV in (a) and 398.8 and 400.0 eV in (b).

The N 1s feature (Figure 4.10(b)) is more difficult to assign unambiguously, since it is known that N can give broad XPS peaks in some materials. Thus, the feature around 399 eV could be one broad peak from N in a single bonding configuration. Alternatively, the feature can be deconvoluted into two peaks (as shown in Figure 4.10(b)), one at 398.8 eV assigned to sp^3 C-N bonds, and one at 400.0 eV assigned to sp^2 C=N bonds [2,72,80,81,82,83]. However, within our experimental accuracy it is impossible to distinguish between these two alternatives. Also, it should be noted that $C\equiv N$ bonds can also produce 3 peaks in this region,

398.2 eV [84], 398.1 eV [85] and 400.1 eV [86]. However, these assignments have been discounted since they are outside of the experimental accuracy of the XPS spectrometer. The presence of sp^3 C-N in the ablated nanostructures is, again, in agreement with a C_3N_4 structure.

In summary, by combining the results obtained by microcombustion, XRD, TEM, HRTEM, SAED and XPS, it is clear that the formation of crystalline carbon nitride by this novel LP-PLA process has been successful. We believe this is due to the ultrafast quenching of the hot plasma and its interaction with the high-nitrogen-content liquid media. This study shows that LP-PLA is a promising method to synthesize some nanomaterials with special structures which are difficult to be produced by other conventional methods.

§ 4.2.2 Control of self-assembled structures

Our preliminary results [87] for LP-PLA of graphite in ammonia solution indicated that a large variety of carbon nitride nanostructures were produced, depending upon the ablation conditions. To investigate these dependences further, a more detailed study to understand the formation mechanism of nanocrystalline carbon nitride was undertaken [88]. It was found that the size and morphology of the ablation products were a complicated function of laser power, ablation time, and ammonia concentration, and these will be described in the following sub-sections. Different experimental conditions can be used to optimise and control independently the nanocrystals nucleation and orientation.

§ 4.2.2.1 Varying ablation time

Experiments were performed for different ablation times with the laser fluence constant at 75 mJ / pulse and 35% ammonia solution. Figure 4.11(a) shows that spherical particles appeared after only 10 min ablation. The areas highlighted by rectangles in Figure 4.11(a) indicate that some of the particles may be lining up, which suggests that they might subsequently coalesce into a NR. Alternatively, NRs may form by one-dimensional (1D) NP growth (highlighted by circles), as NPs add

preferentially to the ends of a line of NPs. Whichever mechanism is correct, it is clear that NR formation, growth and aggregation all occur on a short timescale. With longer ablation times, the NRs start to aggregate into multilayered structures, serving as the starting points (or nucleation seeds) for the subsequent growth. After ~30 min ablation time we observe (Figure 4.11(b)) a mixture of different sized NPs, some of which have begun to coalesce into leaf-like shapes. As ablation continues, these leaf-like structures increase in size, as can be seen in Figure 4.11(c). Figure 4.11(d) and (e) show that these leaf-like nanostructures are mostly made up of component NPs or NRs. With even longer ablation times (5 h), the length and width of the internal NRs (width ~5-10 nm, length ~30-100 nm) remained almost constant (Figure 4.11(f)), but the number of leaf-like structures increased, with all the well-aligned internal NRs pointing in the same direction, perpendicular to the propagating *c*-axis (Figure 4.11(e-f)).

High-resolution TEM images of a series of aggregated particles are shown in Figure 4.12. It is seen that the lattice planes of the particles are almost perfectly aligned. Some leaf-like structures are interconnected (Figure 4.12(a)) and the lattice planes of each particle are fused directly, with no evidence for an amorphous boundary interlayer (Figure 4.12(b-d)). Although individual leaf-like structures within a local region seem to be randomly oriented, the overall NR aggregates still exhibit long-range ordering [89,90] (Figure 4.12(e)). A representative SAED pattern is given in Figure 4.12(f), showing diffraction spots from the $(\bar{1}10)$, $(\bar{1}\bar{1}0)$, $(\bar{1}01)$ and $(10\bar{1})$ planes of the $[111]$ zone-axis, which are aligned parallel each other. Therefore, a clear crystallographic relationship exists among the $[111]$ -oriented crystallites [91]. Indeed, in Figure 4.12(a-d) most of the observed lattice planes in these images are the (111) plane corresponding to crystalline β -carbon nitride with an interplanar distance of 0.193 nm [92], and which lie perpendicular or parallel to the *c*-axis.

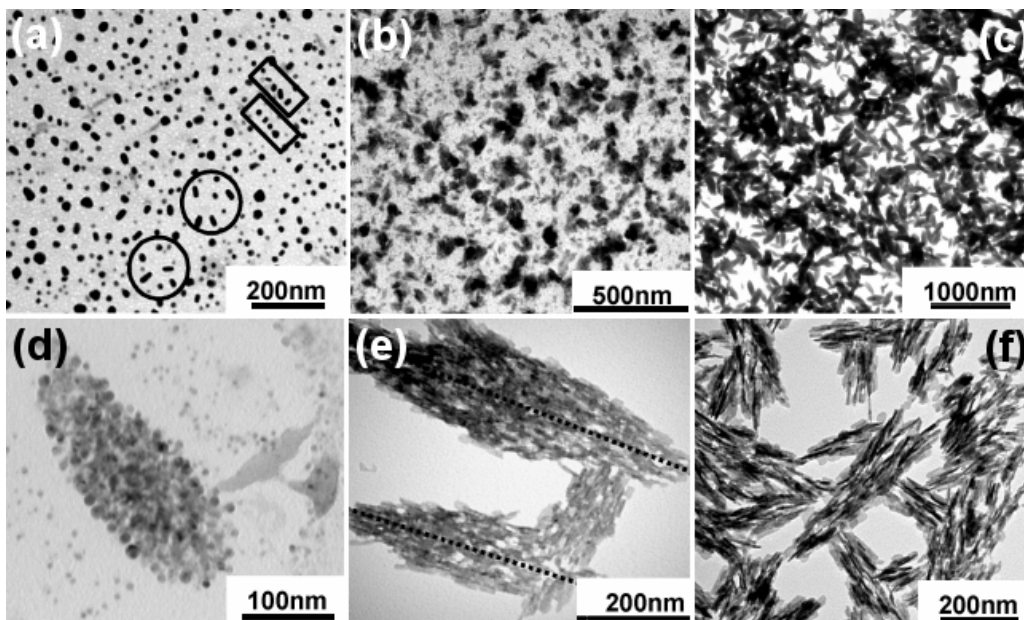


Figure 4.11 TEM images of C_3N_4 nanostructures synthesized at 75 mJ / pulse laser fluence for different ablation times. (a) After 10 min ablation, spherical NPs appear, with an average particle size of 15-20 nm. Adjacent particles are aligned with one another along their main axes, highlighted by the inset rectangles. Short rods (highlighted by circles) have already formed, and serve as the starting structures for the subsequent formation of leaf-like structures. (b) After 30 min ablation there is a mixture of leaf-shaped structures and their component NPs. (c) After 3 h ablation the leaf-like structures are larger, better developed, and have a smooth surface. (d) A single 'leaf' formed by numerous small NPs. (e) Interconnected leaf-like structures formed by NRs. Note that those rods perpendicular to the propagating axis (*c*-axis, dashed line in the picture) along the structure were well aligned. (f) High magnification image showing that after 5 h ablation time the NRs inside the leaf-like structures have not changed in size or shape.

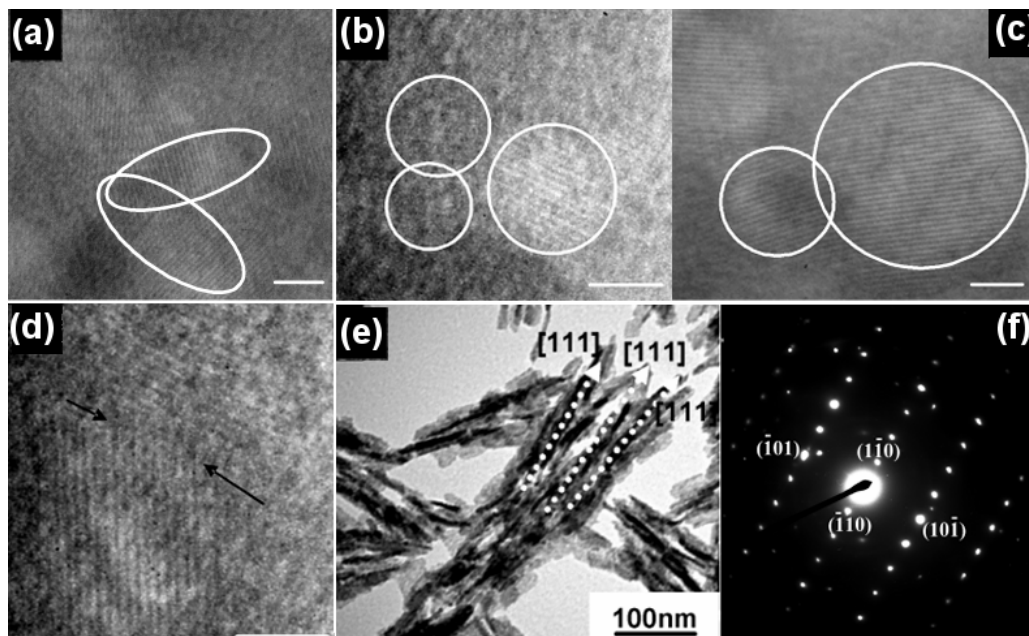


Figure 4.12 (a-d) HRTEM images of a series of aggregated particles, scale bar is 2 nm. (a) The interconnection of two leaf-like structures is highlighted by the two ringed areas. (b) The size of the internal NPs is about 3-5 nm. (c) The lattice planes go straight through the interface between the particles, which means that the particles are fused together with no interlayer separating them. (d) High magnification image of a grain boundary, shown by the arrows. (e) The NR aggregates exhibit a long-range order; arrows in (e) indicate the projecting direction along [111]. (f) SAED pattern of a NR from the [111] zone-axis indicating the area is a single crystal and consistent with crystalline β -carbon nitride.

It was found that the size of the leaf-like structure can be controlled by optimising the conditions, *i.e.*, laser power at 100 mJ. Statistical analysis of the length of the C_3N_4 nanoleaf structures (Figure 4.13(a-d)) yields average lengths $\langle l \rangle$ of 235, 272, 336 and 399 nm for different ablation times $t = 1, 3, 5,$ and 7 h, respectively (Figure 4.13(e)), while the average widths remained roughly constant at 80 ± 20 nm. $\langle l \rangle$ increases in direct proportion to the ablation time until 7 h, at which time the structures begin to aggregate into larger units. For ablation times longer than 7 h, very few isolated nanoleaf structures are observed, with most being

aggregated into disordered micron-scale complex crystallites in an open network. With ablation times >12 h, the nanoleaf structures coalesce to form the ‘flower-like’ structures that would be discussed in the following section.

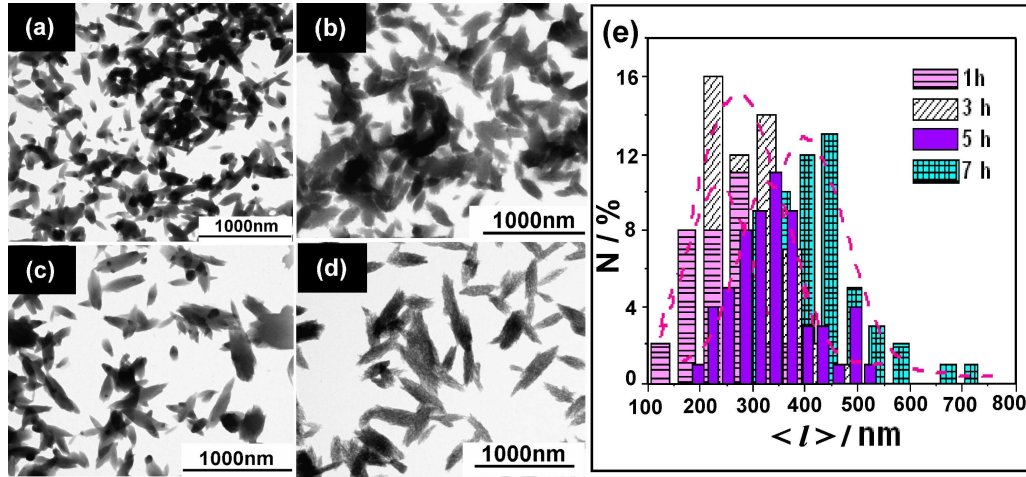


Figure 4.13 TEM images of as-synthesized C_3N_4 nanoleaf structures prepared using a laser fluence of 100 mJ per shot and 35% ammonia solution for ablation times of (a) $t = 1$ h, (b) 3 h, (c) 5 h and (d) 7 h. The concentration of the nanoleaf structures decreases with ablation time, but the average length of each nanoleaf increases. (e) The corresponding nanoleaf length distribution for samples grown under different ablation times (with Gaussian fits to the data, dashed lines), as determined from TEM images. N = number fraction of nanoleaf structures, expressed as a percentage. Statistical analysis of the length of the C_3N_4 nanoleaf structures yields average lengths $\langle l \rangle$ of 235, 272, 336 and 399 nm for different ablation times $t = 1, 3, 5,$ and 7 h, respectively.

§ 4.2.2.2 Varying laser fluence

Laser fluence might be expected to have an effect on ablation products, as it has been shown by Devaux *et al.* [93] to be related to the plasma pressure via an experimentally-proven analytical model. This relationship is given, assuming constant laser energy $I(t) = I_0$ throughout the pulse duration, by the equation:

$$P = \sqrt{\left(\frac{\alpha}{2\alpha + 3}\right)} \sqrt{Z} \sqrt{I_0} \quad (4.2)$$

where P is the plasma pressure (constant) in GPa, I_0 is the laser intensity in GW cm^{-2} , α is a correction factor and Z is related to the shock impedance of each material in $\text{g cm}^{-2} \text{s}^{-1}$. Hence, laser fluence is related to the square of the pressure, which may have an effect on ablation products via the conditions present during formation. The plasma energy could be further increased due to laser-supported absorption by the plasma plume.

The initial experimental trial was studied via varying laser fluence with a fixed short ablation time (1 h) and 35% ammonia solution. The nanostructures outlined in Figure 4.14 indicate that laser fluence, indeed, has some effect upon the ablated product. For low laser fluence (25 mJ/pulse), no particular structures can be observed, only some mono-dispersive NPs, probably due to less reaction time and insufficient energy. Figure 4.14(a) shows the as-ablated carbon nitride aggregates at 50 mJ / pulse, which comprise ~ 10 nm in diameter by 80-120 nm long dispersed NRs (the NRs appear dark while other parts are light). On increasing the laser fluence to 75 mJ/pulse (Figure 4.14(b)), it was found that the NRs became longer and arranged themselves radially from centre. A further increase in the laser fluence led to the 1D leaf-like structures as mentioned previously, formed by small NRs attached parallel and side-by-side (Figure 4.14(c)). At 125 mJ / pulse, a new morphology occurred, which can be described as an incomplete semi-sphere with fuzzy NRs around the edge (Figure 4.14(d)). If the NRs were continuously created in the system, they might easily become trapped in the spaces between the NRs around the edge of the semi-sphere, leading to a change in crystal morphology. In the present case, it should be expected that at high reaction rates (*i.e.* for longer ablation times and/or higher laser fluence) well-controlled complex morphologies could be more readily produced because of a rapid increase in supersaturation and continuous supply of reaction groups over a long period of time.

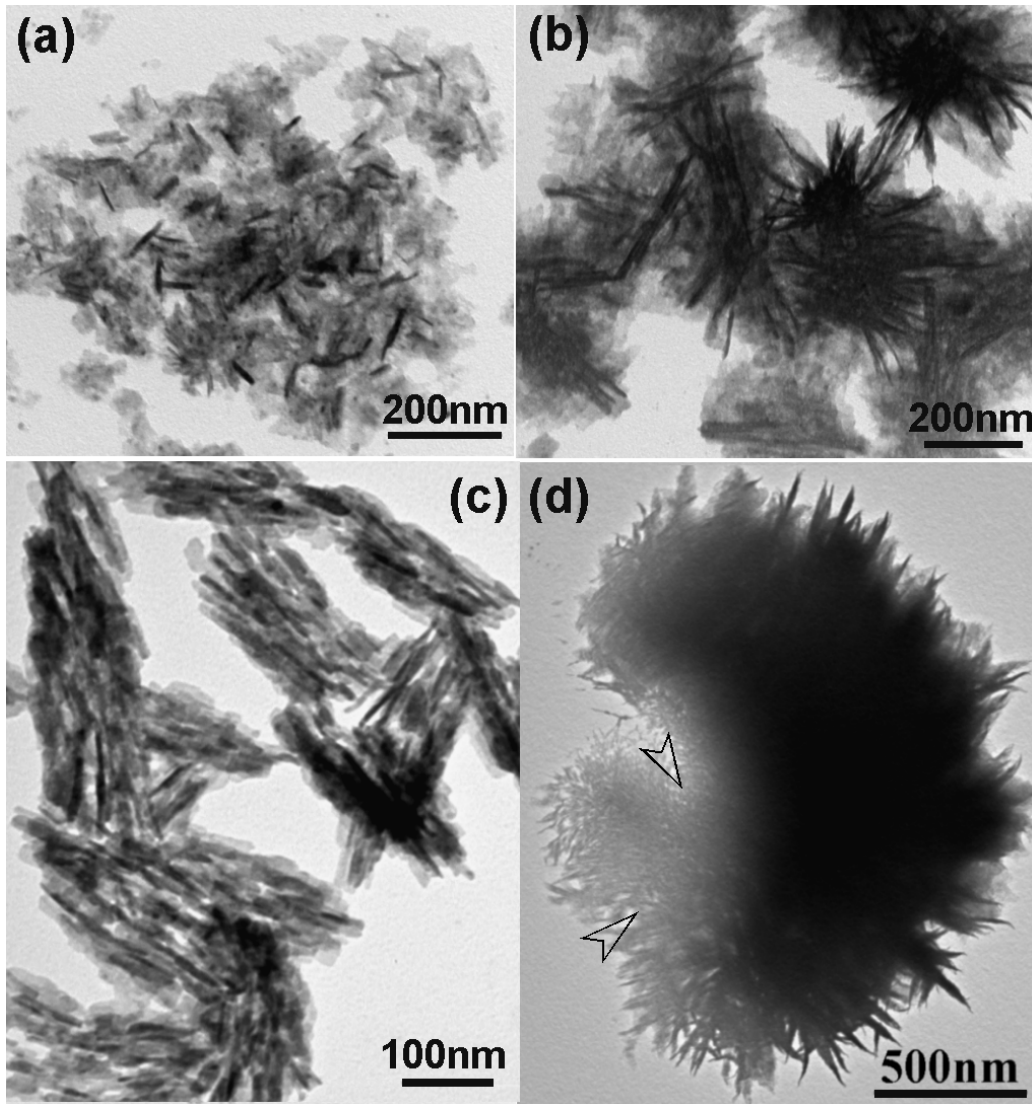


Figure 4.14 TEM images of C_3N_4 nanostructures synthesized for 1 h ablation time and 35% ammonia solution using different laser fluences. (a) 50 mJ/ pulse, (b) 75 mJ/ pulse, (c) 100 mJ/ pulse, (d) 125 mJ/ pulse, arrowhead marked the boundary area between the semi-sphere and the small ball (see text for the discussion).

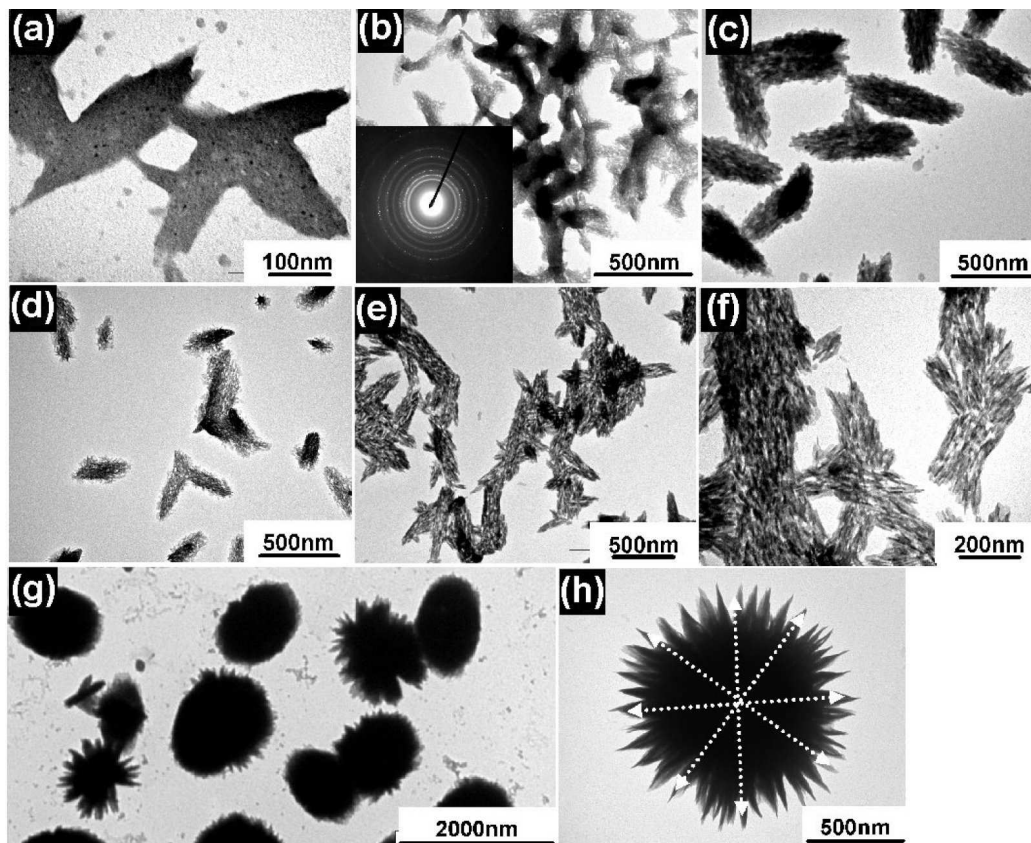


Figure 4.15 TEM images of C_3N_4 nanostructures synthesized for 3 h ablation time and 35% ammonia solution using different laser fluences. (a) and (b) 25 mJ/ pulse, leaf-like structures containing spherical NPs. Inset in (b) is a sharp SAED pattern indicating the structures are crystalline. Note that there appear to be voids inside the leaf-like structures (the white areas in the grey area of image (b)). (c) and (d) 50 mJ/ pulse, denser leaf-like structures containing longer NRs which protrude from the surface. (e) and (f) 75 mJ/ pulse, leaf-like structures beginning to aggregate into larger clumps. (g) and (h) 100 mJ/ pulse, carbon nitride nanospheres and flower-like spiky crystallites.

The effect of different laser energies was also investigated with longer constant ablation time (3 h) but keeping the same ammonia concentration (35%). Figure 4.15 summarises the different C_3N_4 nanostructures synthesized with varying laser fluences. For low laser fluence (25 mJ/pulse), the leaf-like structures had a length

and width of ~ 300 and ~ 120 nm, respectively, with smooth surfaces, and were composed of smaller-sized NPs (Figure 4.15(a)). There were also plenty of voids situated between some of the NPs (Figure 4.15(b)). The sharp SAED pattern for the leaf-like structures (inset Figure 4.15(b)) was consistent with crystalline hexagonal β -phase carbon nitride [76,92]. When the laser power was increased to 50 mJ / pulse, the aligned leaf-like structures increased to a length and width of ~ 600 and ~ 250 nm, respectively (Figure 4.15(c-d)), and now consisted of a substantial number of connected NRs. The surface of the leaf-like structure was no longer smooth, but contained numerous protruding NRs. For still higher fluences (75 mJ / pulse), there was no further significant change in the size or shape of the leaf-like structures and NR building units (Figure 4.15(e-f)), but there was an increase the number formed. With further increases in fluence to 100 mJ per pulse, micron-scale carbon nitride spheres (Figure 4.15(g)) were observed, which were formed following aggregation of a large number of the leaf-like structures. ‘Flower-like’ spiked crystallites (Figure 4.15(h)) were also seen, where the leaf-like structures coalesced at a common centre with multi-fold symmetry [94]. In general, the trend is that the size of the overall nanocrystallites and their basic building blocks increases with increasing laser power.

As mentioned in section 4.2.2.1, with ablation times >12 h, the nanoleaf structures coalescing to form the ‘flower-like’ structures become a common case. Figure 4.16 reveals the TEM images at 12 h ablation of differently-developed carbon nitride flowers. At 50 mJ/pulse, an individual flower (Figure 4.16(a)) usually exhibited a surface composed of NRs, where the NRs radiate outward from the centre. At higher laser fluence (75 mJ/pulse), an underdeveloped flower-like morphology composed of leaf-like building blocks could be observed (Figure 4.16(b)). However, it is interesting to see a fully developed carbon nitride flower (Figure 4.16(c)) similar to that shown in Figure 4.15(h) when the laser power was increased to 125 mJ / pulse. The laterally-fused NRs have diameters in the range of 10-20 nm and lengths of 150-300 nm. The results indicate that the formation of the flowers may be due to the higher plasma pressure induced by the higher laser fluence causing further ablation, material reaction with the liquid phase and/or nanostructure growth. Longer ablation time also gave the small building blocks sufficient energy

and timescale to preferentially orient themselves, eventually forming the structures observed here. It is noteworthy to stress that these flower structures are rather stable - they could not be destroyed even after many hours of sonication.

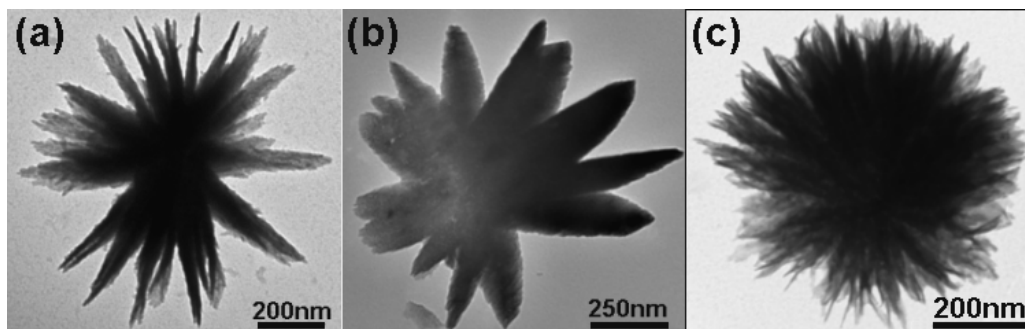


Figure 4.16 TEM images of C_3N_4 nanoflowers synthesized for 12 h ablation time and 35% ammonia solution using different laser fluences. (a) 50 mJ/ pulse, (b) 75 mJ/ pulse, (c) 125 mJ/ pulse (see text for the discussion).

§ 4.2.2.3 Varying ammonia concentration

When 35% ammonia was replaced by 25% ammonia solution, carbon nitride was still formed; however, the morphology was different under TEM observation. For low laser power (50 mJ) and short ablation time (1 h), the product contained mostly a sparse collection of isolated NRs (Figure 4.17(a)). With longer ablation times (3 h), the NRs started to aggregate into branched structures (Figure 4.17(b)), serving as the starting points (or nucleation seeds) for the subsequent growth. Such rod-like aggregates were different from those prepared at 35% ammonia solution, mainly leaf-like structures contained numerous protruding NRs (see Figure 4.15(c) and (d)). With increasing laser power (100 mJ) and ablation time (12 h), the concentration of NRs increased, and highly-branched flower-like architectures completely composed of NRs can be observed (Figure 4.17(c)). The NRs at the edge of the flower structures appeared to be protruding outward by ~ 10 nm. As shown in Figure 4.17(d-e), it should be pointed out that these NRs are themselves composed of a large number of smaller NPs that have packed together in an ordered arrangement

to form the rod-like shapes. In particular, in the HRTEM image in Figure 4.17(f), taken from a single NR, the periodic lattices clearly show the atomic arrangement (Figure 4.17(f) inset) with very few defects, and reflect the relationship between the orientation of the NPs and the crystallography of the ordered NR array.

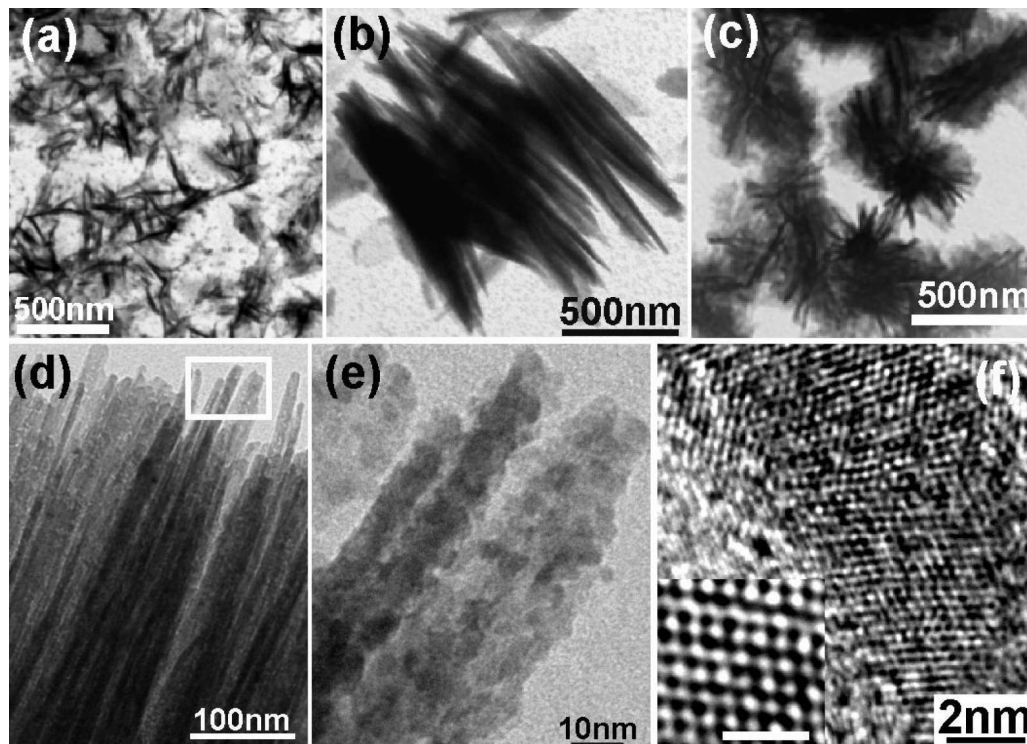


Figure 4.17 TEM images obtained by LP-PLA in 25% ammonia solution: (a) isolated carbon nitride NRs (50 mJ/ pulse, $t = 1$ h) (b) Branched NRs (50 mJ/ pulse, $t = 3$ h) (c) highly branched flowerlike architectures (100 mJ/ pulse, $t = 12$ h). (d) Rod-like structures showing straight, long and sharp tips. (e) Enlarged image of the region at the top of the NRs indicated by the open box in (d). (f) HRTEM image of a single NR, the inset shows the atomic arrangement, scale bar 1 nm.

§ 4.3 Properties of carbon nitride

§ 4.3.1 Vibrational properties via Raman spectroscopy

Illustrative Raman spectra from the carbon nitride nanocrystallites at different ablation times are given in Figure 4.18, showing broad features at $\sim 1600\text{ cm}^{-1}$ and 1380 cm^{-1} . For amorphous carbon, graphite, or CN_x films, these features would correspond to the well-known G and D bands, respectively [95]. However, similar features would also be expected in the Raman spectra from the hexagonal lattices of both α - and β - C_3N_4 [96,97,98].

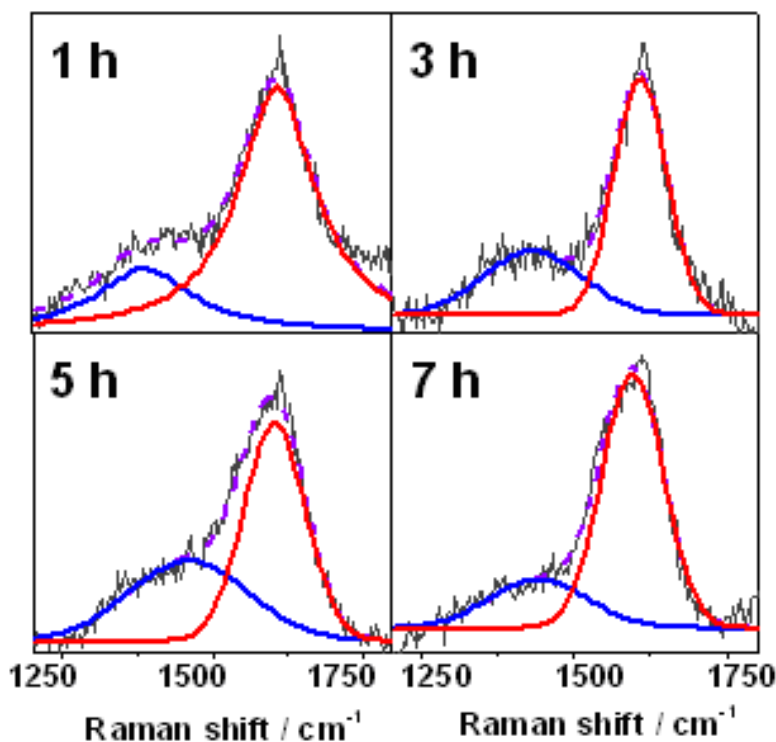


Figure 4.18 Raman spectra (325 nm excitation wavelength) from the C_3N_4 leaf-like structures following different ablation times at 100 mJ per shot laser fluence. The spectra are fitted in terms of two independent Gaussian functions (solid curves) centred $\sim 1600\text{ cm}^{-1}$ ('G band') and $\sim 1380\text{ cm}^{-1}$ ('D band'), respectively, after subtracting a linear contribution for background fluorescence.

According to the empirical model for amorphous carbon proposed by Ferrari and Robertson [99], the wavenumbers of the G and D band maxima, G_{\max} and D_{\max} , and the ratio of their peak intensities, $I(D)/I(G)$, can be used to gain information about structure and disorder within such materials. Each spectrum was therefore deconvoluted using a Gaussian fit into the carbon nitride equivalents of graphitic D and G vibration modes.

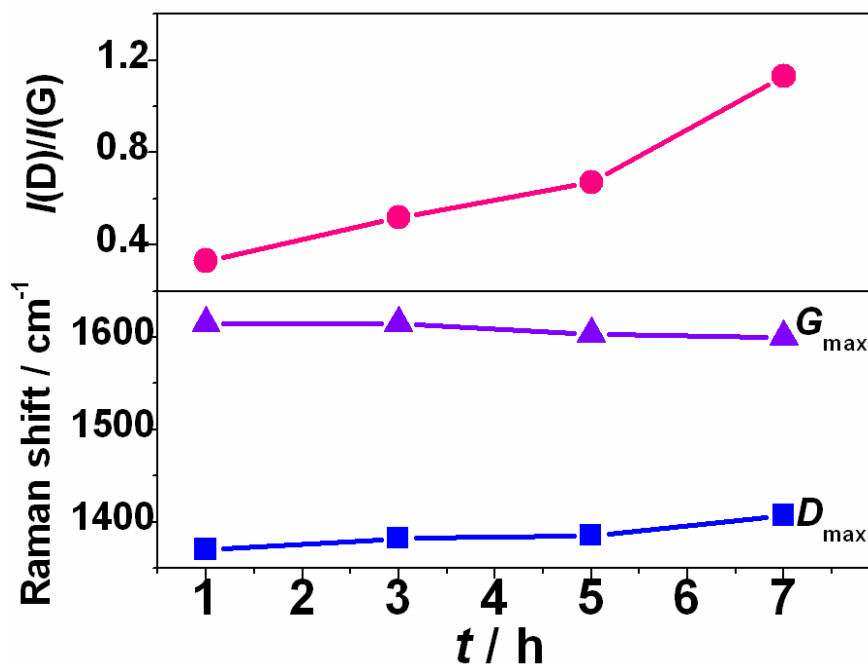


Figure 4.19 Plots showing the variation of G_{\max} , D_{\max} and $I(D)/I(G)$ as a function of ablation time, t , for the carbon nitride leaf-like nanocrystals synthesized by LP-PLA at 100 mJ per shot.

G_{\max} , D_{\max} and $I(D)/I(G)$ as a function of ablation time are shown in Figure 4.19. The $I(D)/I(G)$ ratio increases with increasing ablation time. This can be probably interpreted as an increase in the size of sp^2 clusters [100]. D_{\max} is seen to shift to higher wavenumber as ablation time is increased while G_{\max} decreases only slightly. The shift of the D band may indicate an increase in the number of carbon sp^3 bonds linking with N atoms [101]. This would result in an increase in the ratio of sp^3 -to- sp^2 bonds [102], which is consistent with the production of C_3N_4 . Lee *et al.*

[103] found that the G band for carbon materials shifts to higher energy ($> 1580 \text{ cm}^{-1}$) with improving crystalline quality, and to energies ($< 1575 \text{ cm}^{-1}$) for amorphous materials. The G band position for our samples does not change significantly with ablation time, indicating that the overall crystallinity of the samples remains constant. This is because the nanoleaf structures are not crystalline themselves, but are composed of an ordered arrangement of crystalline NRs. Increasing the ablation time increases the number of NRs in each nanoleaf, but does not change the crystallinity of the nanoleaf itself.

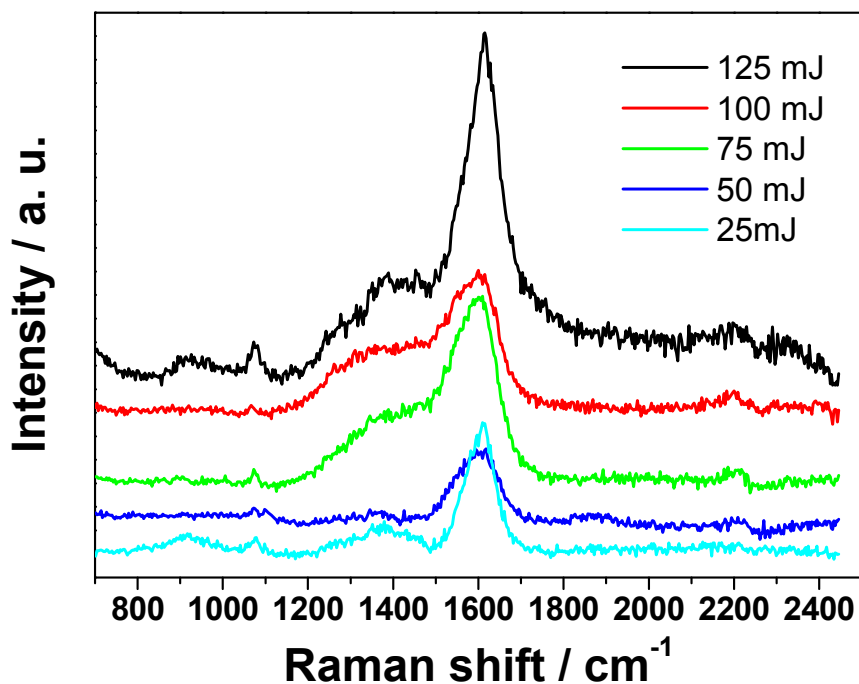


Figure 4.20 Raman spectra for the C₃N₄ nanostructures following different laser fluence experiment, *i.e.* $t = 3$ h ablations at 125, 100, 75, 50 and 25 mJ/pulse, respectively.

Raman spectroscopy was also performed for the products prepared at various laser fluences, with results given in Figure 4.20. The higher fluence ablations of 125, 100 and 75 mJ produced spectra with both D and G bands, however the lower

fluence 25 and 50 mJ ablations showed spectra with the G band only. Hence, this may indicate that in the lower fluence ablations the final products contained mainly graphite powder and very little nitrogen had been incorporated into the material to form C-N bonds. Therefore, production of carbon nitride depends on laser fluence, with a threshold energy of between 50-75 mJ. This is in good agreement with the TEM observations that the uniform and ordered carbon nitride morphologies are only found at high laser power (>50 mJ per pulse). This trend is further seen as $I(D)/I(G)$ increases markedly for the 125 mJ ablation, which indicates an increase in the relative C_3N_4 yield. A wider scan range shows a small peak at $\sim 2250\text{ cm}^{-1}$ for all the laser fluence assigned to $C\equiv N$, which is evidence for direct carbon-nitrogen bonding in the system, although possibly as impurities rather than as part of the crystal lattice.

§ 4.3.2 Bonding state via XPS analysis

XPS measurements estimated that the overall elemental composition of the nanoleaf structures was 86.3% C, 11.4% N, and 2.3 %O after 5 h at 100 mJ per shot laser fluence, whereas for 7 h ablation values were 90.5% C, 7.8% N and 1.7%O. One possibility for the presence of the O signal is that the graphite target reacted directly with the water (or OH radicals generated in the water) during the high temperature conditions in the ablation plume. However, since the O signal decreased with longer ablation time, this idea has been discounted. An alternative explanation is that prolonged exposure of the samples to the laboratory atmosphere led to possible contamination by absorbed or adsorbed water vapour. For pure C_3N_4 , we would expect a composition of 42.8% C and 57.2% N, which shows that our samples are considerably carbon rich. Since we know from TEM observations that regions of the samples contain pure C_3N_4 , we must conclude that our samples are a composite of crystalline C_3N_4 and an amorphous carbon background. This observation is consistent with the conclusions by other workers [24,104], who found that it was difficult to generate highly ordered structures containing large concentrations of N incorporated into the C network.

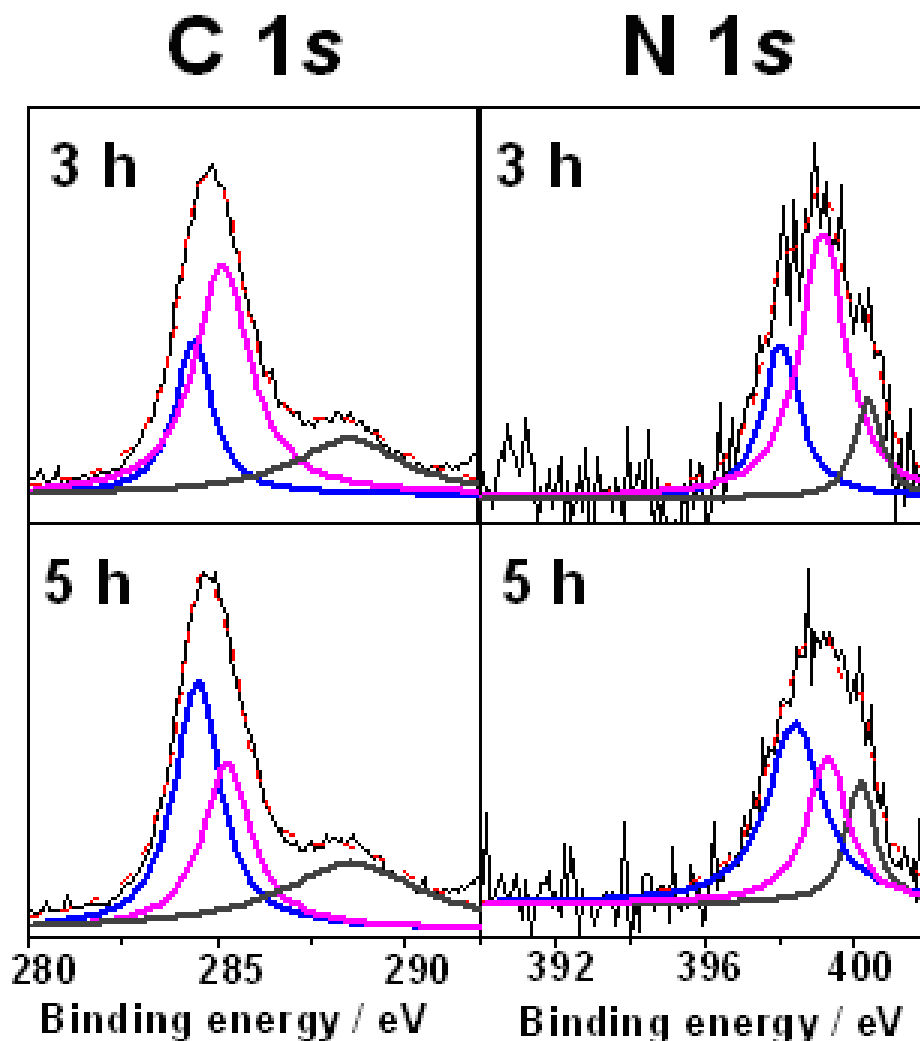


Figure 4.21 C (1s) and N (1s) XPS spectra of C_3N_4 nanostructures for different ablation times. Each spectrum has been deconvoluted by fitting to three Gaussian lineshape functions, with the total fitted line overlaid as a dashed (red) line.

The breadth and asymmetry of the C (1s) and N (1s) core-level XPS spectra shown in Figure 4.21 indicate the presence of different bonding states within the crystallites. The core-level lines were fitted to a Gaussian function [105]. The N 1s feature is difficult to assign unambiguously, since it is known that N can give a broad XPS peak around 399 eV in some materials. Alternatively, a better fit can be achieved if the feature is deconvoluted into three peaks (as shown in Figure 4.21), located at ~ 398.5 eV, ~ 399.6 eV and ~ 400.2 eV, respectively. The peaks situated at

~398.5 eV can be assigned to sp^3 C-N bonds, and one at 400.2 eV assigned to sp^2 C=N bonds [106]. A peak centred at a binding energy ~399.6 eV has been assigned by some groups [107,108] to N atoms bonded to sp -hybridized C atoms (*i.e.* -C≡N). These assignments are also supported by *ab initio* binding-energy calculations [109]. Nevertheless, within experimental accuracy it is impossible to distinguish between these two alternatives. Also, it should be noted that C≡N bonds can produce 3 peaks in this region [108], 398.2 eV [84], 398.1 eV [85] and 400.1 eV [86]. However, these assignments have been discounted since they are outside of the experimental accuracy of the XPS spectrometer. The presence of sp^3 C-N in the ablated nanostructures is, again, in agreement with a C_3N_4 structure.

Similarly, the C 1s core-level spectra obtained by XPS (Figure 4.21) was deconvoluted into three peaks located at ~284.6 eV, ~285.5 eV and ~288.5 eV, respectively. However, unlike nitrogen, verification of the assignment by independent C (1s) spectra was relatively difficult due to the small shifts in binding energy and the multiple bonding environments of the carbon. Carbon atoms may have zero, one, two, or three bonds with nitrogen atoms, which complicate the situation, so that there is a wide range of interpretation in the literature for carbon spectral feature identification. The peaks at ~284.6 eV and ~285.5 eV can be identified unambiguously as sp^2 and sp^3 hybridized carbon [110,80,81]. But the assignment for the peak at ~288.5 eV has not yet reached a consensus. In our case, it is believed this peak corresponds to N≡C sp bonding [86] supported by the previous Raman data. Le Normand *et al.* [83] have claimed that it is inappropriate to assign components appearing at higher energies to specific C-C or C-N bonding environments. After searching a comprehensive range of organic polymers, Beamson and Briggs [111] also found that no significant difference in C 1s position can be appreciated between sp^2 and sp^3 -hybridized carbon bonded to nitrogen.

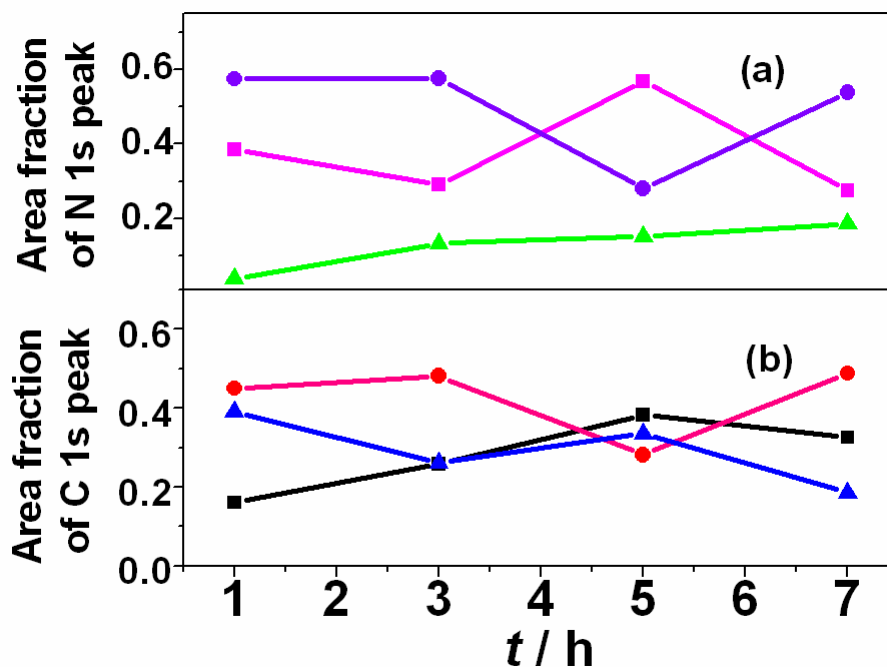


Figure 4.22 Plots showing the time dependencies of the relative areas of the Gaussian functions used to fit (a) the N (1s) XPS peak (key: ■ 398.5 eV sp^3 C-N bonds, ● 399.6 eV C≡N bonds, ▲ 400.2 eV sp^2 C=N bonds), and (b) the C (1s) XPS peak (key: ■ 284.6 eV, ● 285.5 eV, ▲ 288.5 eV).

The relationship between ablation time and relative N 1s peak area fraction is shown in Figure 4.22(a). The peak area corresponding to N=C (sp^2) bonding indicates a marked increase with prolonged ablation time, whereas the trends for C≡N (sp) and N-C (sp^3) are relatively complex. Nitrogen inclusion into the CN network changes the shape and position of the C 1s peak, as seen as in Figure 4.22(b). However, only the signal attributed to C=C (sp^2) bonding shows smooth variation, *i.e.* increasing with ablation time, while all other signals show a more complicated trend.

XPS results for different laser fluence were also tried but did not yield good results because of limited access to the XPS spectrometer, and fresh ablated material and sufficient yields are also needed to obtain reliable results.

§ 4.3.3 Optical properties of the nanostructures

The UV-visible absorption spectra of the ablated solutions after different ablation times (laser fluence at 100 mJ /pulse) are shown in Figure 4.23, displaying a peak at ~ 266 nm. It is known [86] that the β - and α - C_3N_4 phases both contain aromatic 1,3,5-triazine rings, which exhibit absorption around 250 nm due to a π - π^* electronic transition. Hence, the experimental 266 nm absorption peak could indicate the presence of one or more of these phases of C_3N_4 within the ablated material. Interestingly, this peak is red-shifted with increasing nanocrystal size [112]. For example, the peak position changes from 266 nm to 269 nm for $t = 1$ h and $t = 5$ h, respectively. From Figure 4.13(e), this corresponds to a mean nanoleaf length change from 235 to 336 nm.

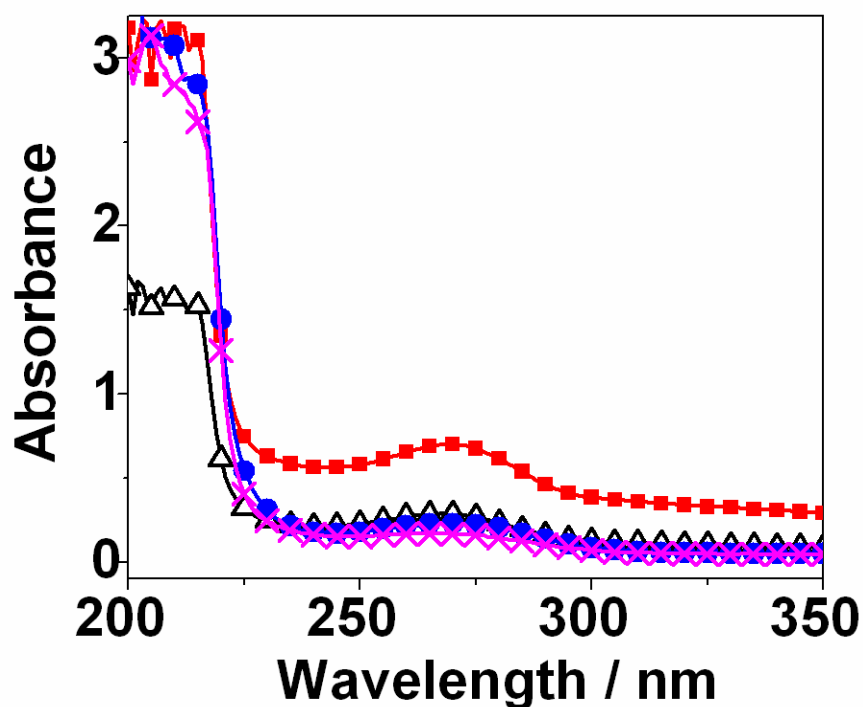


Figure 4.23 Plot of UV-visible absorbance from the ablation product (laser fluence at 100 mJ /pulse) for different ablation times, showing a prominent feature at ~ 266 nm. Key: \blacksquare 1 h, \triangle 3 h, \bullet 5 h, \times 7 h.

Since carbon nitride is predicted to be semiconducting, the onset of absorption will give the optical (or Tauc) band gap of the material, which can be found as the wavelength at which the extrapolation of the steeply-rising part of the absorption spectrum crosses the wavelength axis. Using Figure 4.23, we can estimate the threshold absorption wavelength and calculate a Tauc bandgap [113], which is shown as a function of ablation time in Figure 4.24. The products had a calculated bandgap around 3.9 ± 0.1 eV and compare favourably with the literature values for the predicted bandgap for α - C_3N_4 and β - C_3N_4 of 3.85 and 3.25 eV, respectively [3]. As can be seen in Figure 4.24, the bandgap of the carbon nitride leaf-like structures held in solution increases smoothly with ablation time, *e.g.* from 3.90 eV after 1 h to 3.97 eV after 7 h. Notably, our C_3N_4 solution remained stable over two months with no sediment forming, thus these unique nanostructures with a tunable direct bandgap ~ 4.0 eV might be materials that are suitable for optical applications.

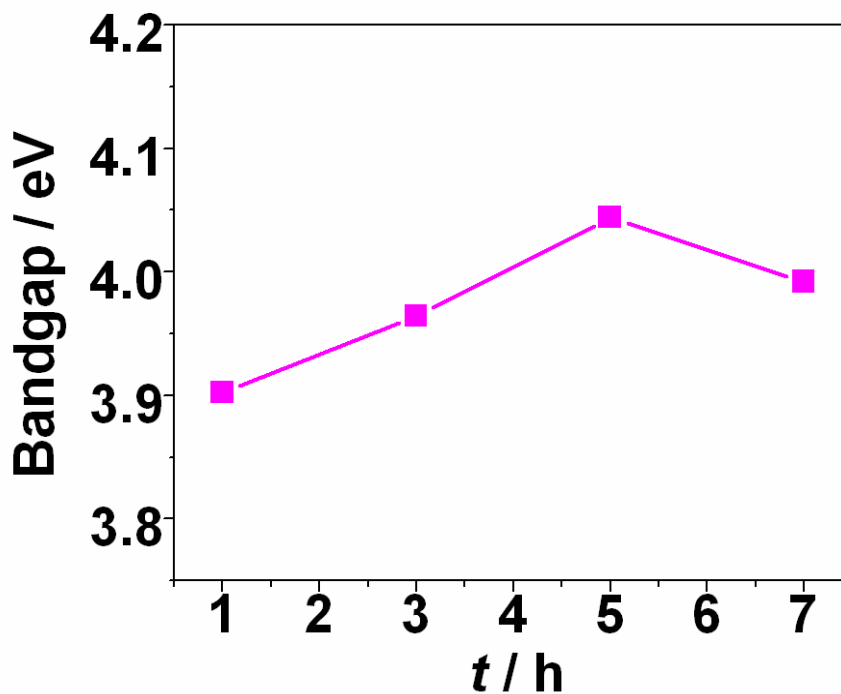


Figure 4.24 Time-dependent relationship of the calculated Tauc band-gap corresponding to different ablation times.

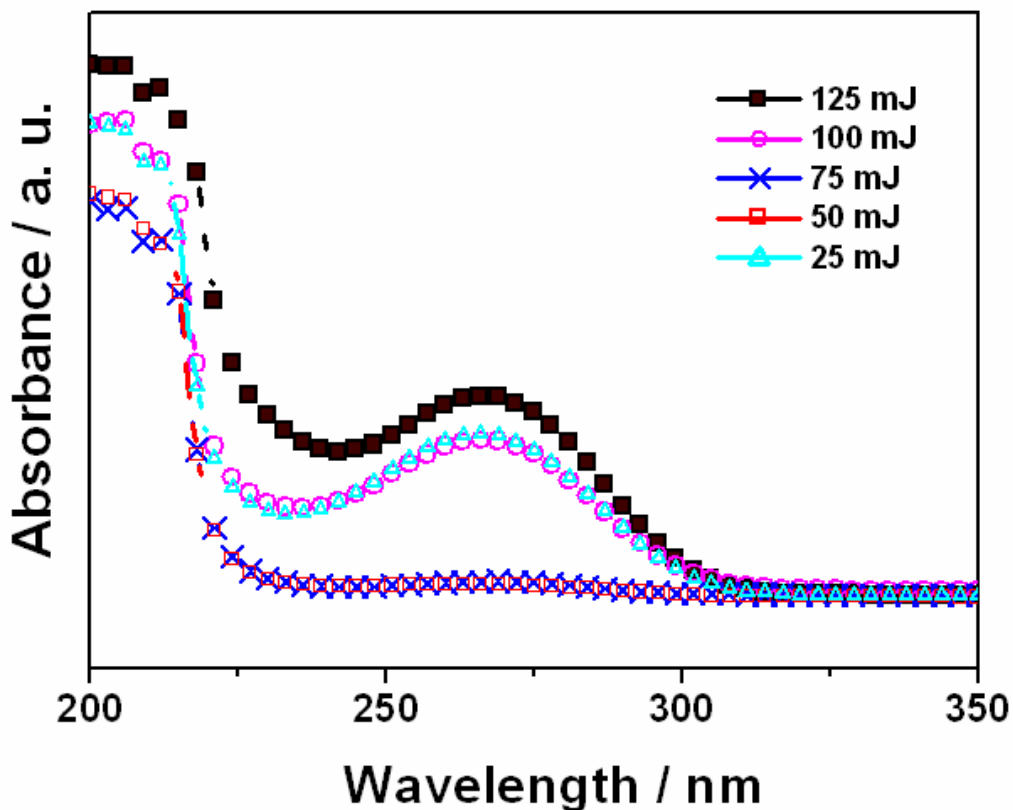


Figure 4.25 Plot of UV-visible absorbance from the ablation product (3 h ablation) for different laser fluence, showing a prominent feature at ~ 266 nm. Key: ■ 125 mJ, ○ 100 mJ, × 75 mJ, □ 50 mJ, △ 25 mJ.

Table 4.4 UV-vis spectroscopy peaks from Figure 4.25.

	Laser Fluence / mJ				
	125	100	75	50	25
Peak / nm	266	266	269	264	265

The UV-Vis data for various laser fluence experiment (Figure 4.25) shows 125, 100 and 25 mJ ablations to have the highest absorbance. It also indicates the peaks to have approximately the same wavelength with different laser fluences. When comparing the peak position (Table 4.3) a slightly increase in wavelength occurs

with an increase in the laser fluence, although the absorbance peak position was greatest in the 75 mJ samples.

As an increase in fluence is unlikely to cause a decrease in sp^3 carbon content, the shift in wavelength of the optical absorption edge can be attributed to an increase in particle size [114]. This is reasonable, as the higher laser fluence may allow ablation of larger graphite particles. Alternatively, the higher pressure and/or effect of laser assisted absorption by the plasma, may cause further material reaction and growth to produce larger nanostructures. Indeed, previously (section 4.2.2.2) we observed an increase in average nanostructure sizes with an increase in laser fluence. Furthermore, there is a trend for higher fluences to have higher UV-Vis absorbance peaks, and hence produce more material. This may be due to higher plasma pressure causing further ablation, material reaction with the liquid phase and/or nanostructure growth. The latter two points could also be a result of greater laser-assisted plasma absorption via higher laser fluences. However, the trend is only approximate due to the high 25 mJ yield in Figure 4.25. This could be attributed to the difficult nature of material collection, *i.e.* material can be lost through transfer and settling, or gained through contamination from ablated material in the cell.

§ 4.4 Growth mechanism for solid-liquid growth

§ 4.4.1 Species diagnostics during laser ablation process

The characteristics of the ablated nanostructures are crucially dependent on the properties of the ablation plume, *i.e.* the degree of ionisation and the velocity of the species contained within the plume. In order to investigate the source of the energetic species present during the laser ablation, the constituents of the plasma were measured using optical emission spectroscopy (OES). Figure 4.26 shows a wavelength-resolved emission spectrum of the ablation plume induced by 532 nm laser excitation (35% ammonia solution, 100 mJ per pulse). Emission from atomic C and C^+ is observed as a direct result of the ablation process. But the presence of very sharp atomic H, N^+ and N peaks shows that the ammonia is also being dissociated in

the PLA process, either directly by interaction with the high energy laser, or indirectly as a result of reactions with the high-kinetic-energy ejected atoms and particles in the plume. Such intense plume reactions have been seen previously during PLA of graphite in vacuum or in gaseous nitrogen or argon backgrounds [115,116].

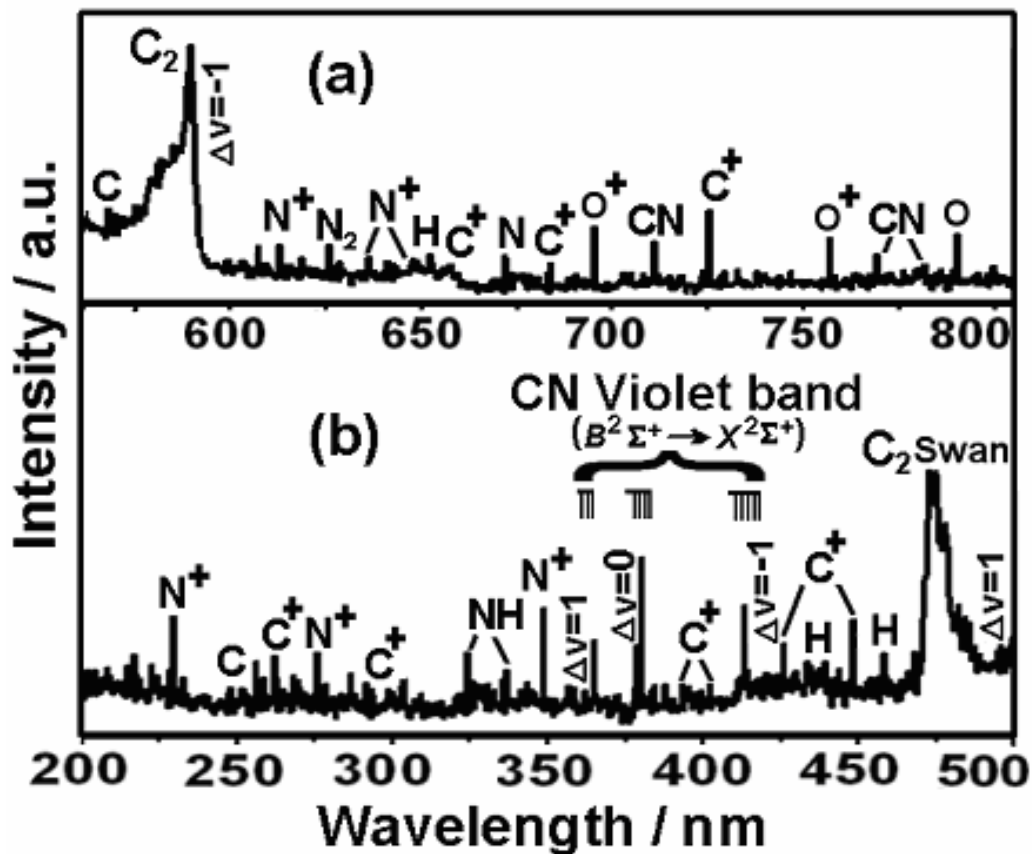


Figure 4.26 A wavelength-dispersed optical emission spectrum of the plume accompanying 532 nm LP-PLA of graphite in 35% ammonia solution. The spectrum has been split into two halves, (a) and (b), either side of the intense reflected laser peak at 532 nm (not shown). The features have been assigned to C_2 ($d^3\Pi_g \rightarrow a^3\Pi_u$, $\Delta v = 1,-1$), CN ($B^2\Sigma^+ \rightarrow X^2\Sigma^+$, $\Delta v = 1,0,-1$), NH, atomic H, N, and C, and C^+ and N^+ ions (using literature values [115,116] as a reference).

In the spectral range 350-425 nm, intense emission from the CN Violet band was observed, and this confirms that a reaction has occurred between carbon atoms from the ablated solid and N from the liquid ammonia. The spectrum also displays strong C₂ Swan band emission. The highly energetic CN and C₂ species in the ablation plume may serve as potential sources for carbon and nitrogen combination [3, 117]. When CN species reached the supersaturation level, heterogeneous nucleation in such short time might result in the self-assembly of the hierarchical superstructures described here. Further investigation of this proposed mechanism is required.

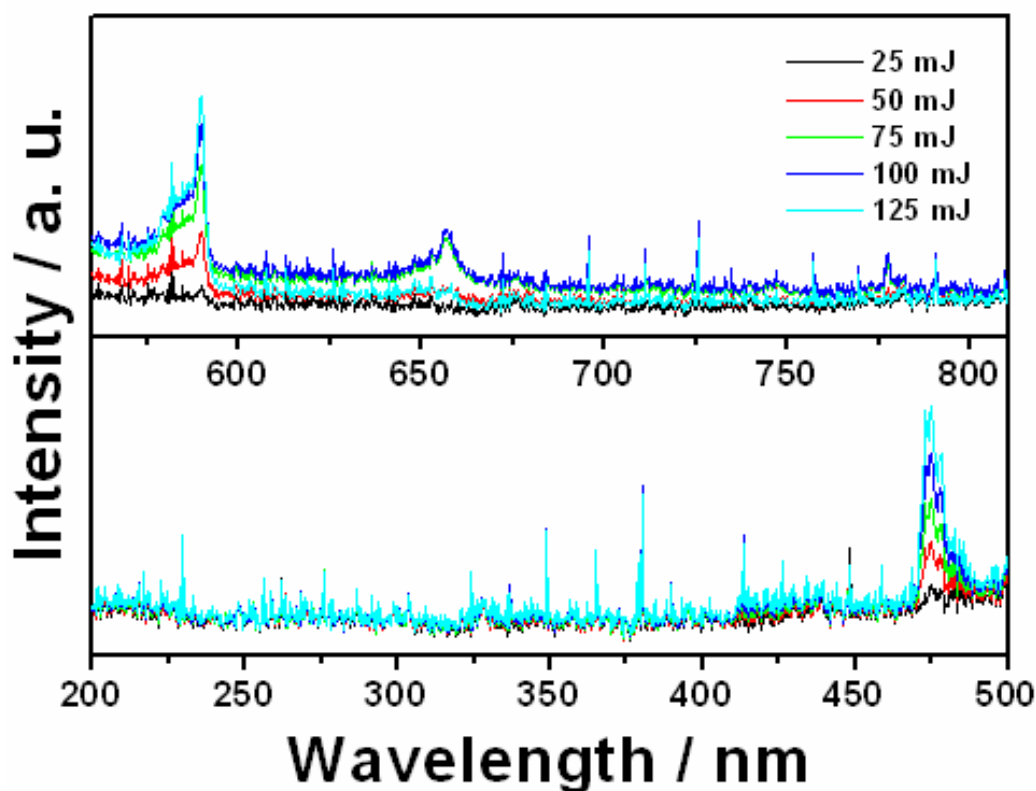


Figure 4.27 The laser fluence dependence of the wavelength-dispersed optical emission spectra of the plume accompanying 532 nm LP-PLA of graphite in 35% ammonia solution. The spectra have been split into two halves, (a) and (b), either side of the intense reflected laser peak at 532 nm (not shown). The assignment of the different peaks is the same as Figure 4.26.

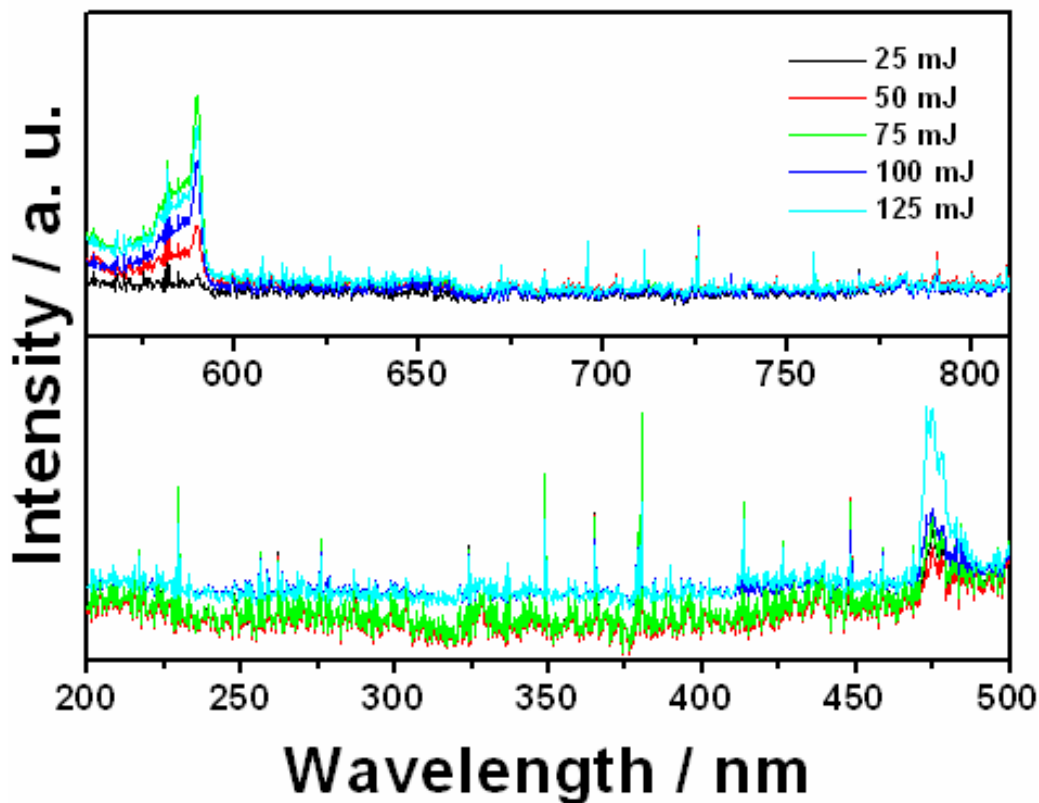


Figure 4.28 The laser fluence dependence of the wavelength-dispersed optical emission spectra of the plume accompanying 532 nm LP-PLA of graphite in 25% ammonia solution. The spectra have been split into two halves, (a) and (b), either side of the intense reflected laser peak at 532 nm (not shown). The assignment of the peaks is the same as Figure 4.26.

After a laser pulse, the species within the plume emit light as they relax from excited electronic states to lower levels. To gain comprehensive information about the species within the plume, OES spectra were taken under various conditions. All spectra were accumulated over 500 laser shots. Figure 4.27 shows the spectra for ablation at the graphite-35% ammonia solution interface with various laser fluences. The peak identification is the same as Figure 4.26. It is clear that the major peaks C_2 , CN, NH, atomic H, N, and C, and C^+ and N^+ ions become much stronger when increasing the laser fluence. Interestingly, the peaks related to the C_2 Swan band and C_2 (d-a) around 580 nm for 25 mJ are very weak compared with other laser fluences.

This may be because the laser power density was not sufficient to cause breakdown of the graphite. In fact, it has been confirmed (see section 4.2.2.2) that the possibility of a power threshold may exist for successful PLA in this system.

A comparable experiment was performed, but with 25% ammonia solution. The spectra were recorded and shown in Figure 4.28. Both studies observe that the C₂ molecular emission becomes predominant. This illustrates that the excited dicarbon radicals are formed via collisional processes. The trend is almost the same as that in Figure 4.27, *i.e.* increasing the laser fluence increases the intensity of the peaks, although the correlation is not as good as that in Figure 4.26. For example, the C₂ peaks ~580 nm had the strongest intensity for 75 mJ per pulse. However, this variation can be explained by experimental error. Another difference between Figure 4.27 and Figure 4.28 involved the peaks ~650 nm for C⁺ and N⁺ ions. In 35% ammonia solution, especially for 75, 100 and 125 mJ, there appeared very obvious sharp peaks within the spectra. This is reasonable because the more concentrated (35%) the ammonia solution; the more N⁺ ions are created during the laser irradiation. Furthermore, high laser energy induces a higher-pressure region (see equation 4.2), which may produce the higher carbon mass or nitrogen fragments, thus the higher intensity for emission from C⁺ and N⁺ ions observed in Figure 4.27. Alternatively, larger C_n fragments may undergo collisional dissociation to produce the C₂ fragments. Such high pressure, high temperature, high density conditions induced by the high-energy laser are normally confined to a small region in front of the target. When the free C and N species encounter and collide with the ejected primary particles in the liquid media, this may favour the non-equilibrium conditions for the formation of carbon nitride with special structures, which are impossible to be produced by other normal methods.

§ 4.4.2 Mechanism for the ordering of carbon nitride nanocrystals

§ 4.4.2.1 Self-assembled arrangement within the nanoleaf structures

Before trying to explain the growth model involved for the whole range of unusual nanostructures seen in this system, we would first like to understand

arrangement of the NP and NR building blocks within the nanoleaf structures. The product morphology of this type can be easily controlled, since a 80% of morphological yield (based on 1000 TEM images) of nanoleaf-like carbon nitride was achieved in this work. It was found that the nanoleaf structures are generated by the coalescence and self-assembly of zero-dimensional (0D) NP or 1D NR building blocks, which organise themselves in different ways.

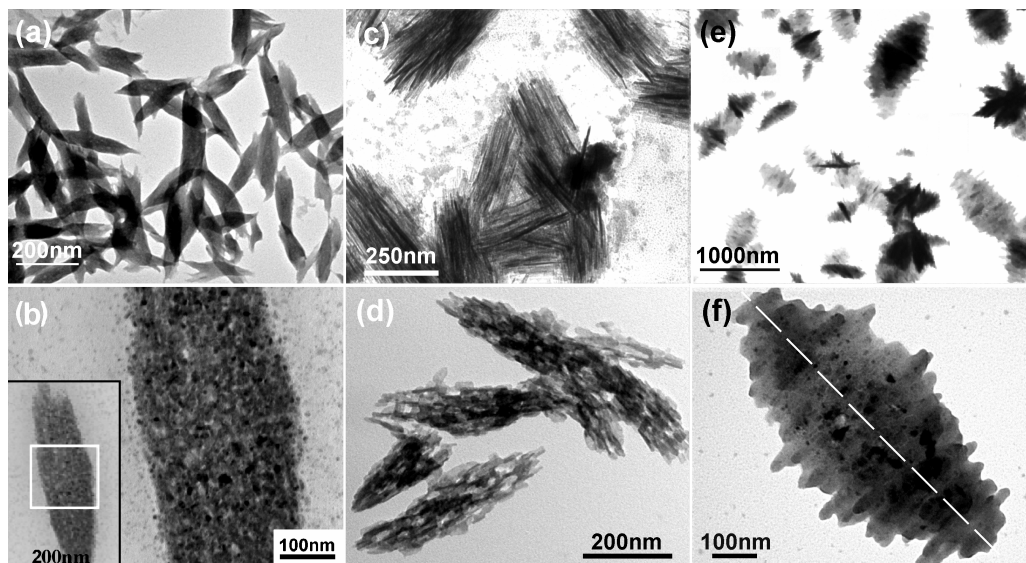


Figure 4.29 TEM images of (a-b) the type (I) organization to form dense leaf-like carbon nitride structures. (b) A single leaf-like unit formed from numerous small NPs (inset area framed with white box). (c-d) type (II) organization with the NRs arranged parallel to the long-axis of the nanoleaf. (e-f) type (III) organization with the NRs arranged perpendicular to the long-axis of the nanoleaf. (f) A single leaf-like type (III) nanocrystallite made from 1D NRs preferentially aligned perpendicular to the long-axis (dashed line).

Figure 4.29 illustrates three types of nanoleaf organisation [118]. The first type (I) of organization is based on a large number of 0D NPs close-packed together to form dense leaf-like structures with smooth surfaces (Figure 4.29(a) and (b)). The second type (II) of organization is obtained when long NR (Figure 4.29(c) or short NR (Figure 4.29(d)) units point in the same direction, and are parallel and well-

aligned along the propagating long-axis. This forms nanoleaves with a rough, less dense surface, with plenty of voids situated between some of the component NRs. Although individual leaf-like structures within a local region seem to be randomly oriented, the overall NR aggregates still exhibit long-range ordering. The third type (III) of organization is more rigidly constructed from numerous closely-packed NRs. Unlike type (II), however, the NRs are now preferentially aligned perpendicularly to the long-axis of the leaf-like aggregates (Figure 4.29(e) and (f)). These nanoleaves have a dense, rough surface. However, it should be mentioned that the latter two cases can be treated as an extension of type (I), because these NRs are themselves composed of numerous smaller NPs that have packed together in an ordered arrangement to form the rod-like shapes (Figure 4.29(d) and (f)).

In explaining the tendency of NRs to align parallel to each other, one reason could be the higher lateral capillary forces along the length of a NR as compared to its width [119]. For spherical particles, it is shown that the lateral capillary force is proportional to R^2 , in which R is the diameter of the particle [120]. This anisotropy of interaction between NRs could be one important driving force for the side by side alignment of NRs rather than end to end. This model seems to explain most of our observed results.

§ 4.4.2.2 Nanoparticle interactions via oriented attachment

Attempts have been made to understand the attachment processes between two or more NPs in our systems, which are essential from the viewpoint of a growth mechanism. It is well known in other NP systems that oriented attachment becomes an important growth mechanism [121]. This involves spontaneous self-organization of adjacent particles so that they share a common crystallographic orientation, followed by joining of these particles at a planar interface. Bonding between the particles reduces the overall energy by removing the surface energy associated with ‘dangling’ bonds (through complete elimination of the solid-air or solid-fluid interface). This mechanism is relevant in cases where particles are free to move (such as in solution or where particles have abundant surface-bound water) and

probably occurs in nature [122]. It may also apply when particles nucleate side-by-side on a substrate and coalesce during growth.

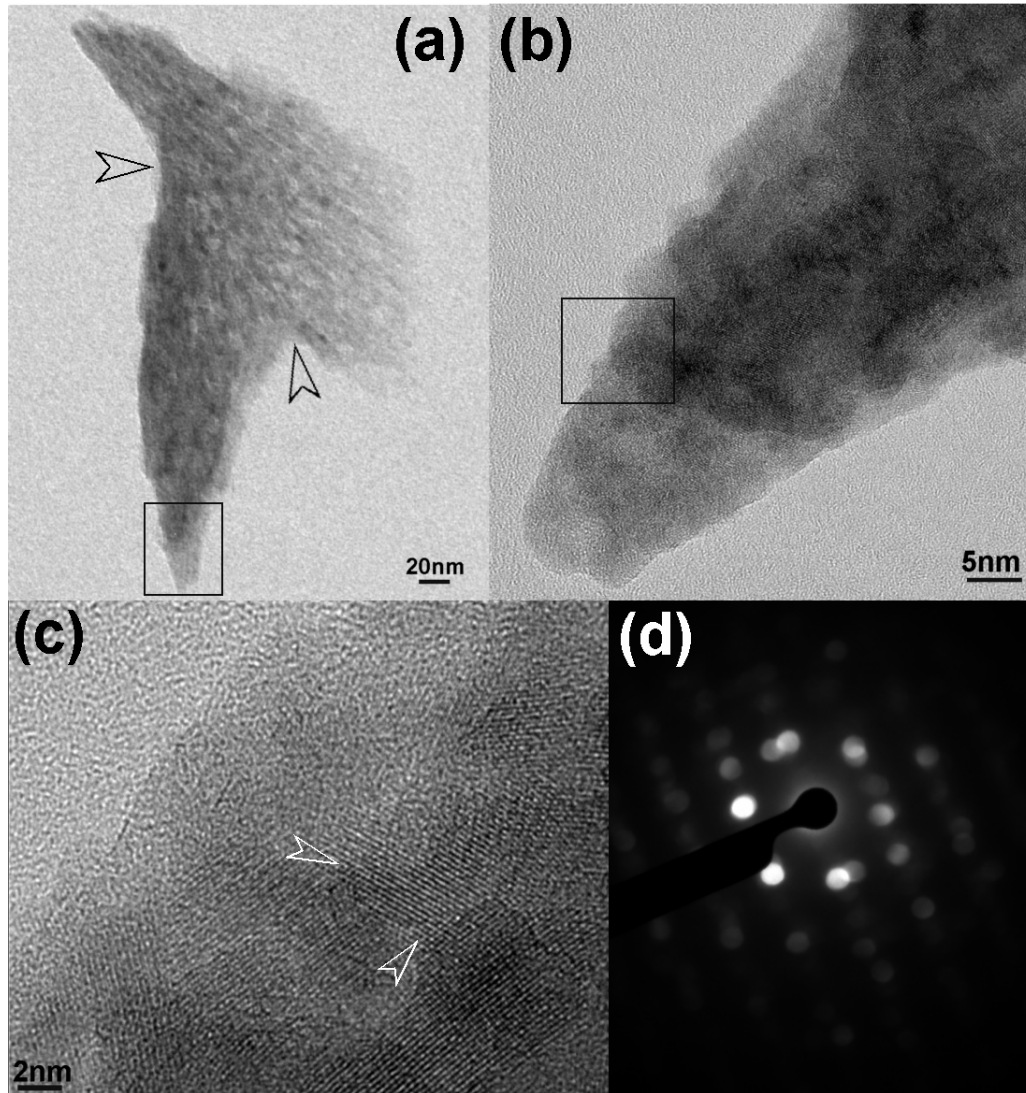


Figure 4.30 (a) TEM image of two carbon nitride nanoleaves. Note that the interconnected boundary is blurred (highlighted by arrowheads). (b) HRTEM image of the tip of the nano-leaf indicated by the open box in (a). It shows an oriented but imperfect attachment of 2 NPs. The dark side indicates that a numbers of NPs rest on the other crystals. (c) HRTEM image of the edge region at the left side of the nanoleaf indicated by the open box in (b). Arrowheads mark the interface between the primary particles. (d) MD pattern from the edge of the nano-leaf in (c).

In our study, we found that particle growth within the liquid media can involve attachment characterized by a small misorientation at the interface, which is referred to as ‘imperfect oriented attachment’. Imperfect oriented attachment of nanocrystals can generate dislocations (line defects) with edge, screw, and mixed character defects. Because the initial nanocrystals were defect free [123], any defects observed by HRTEM can be attributed to the growth process. Imperfect oriented attachment involving multiple particles may result in closely spaced dislocations, possibly leading to the growth of complex long-period structures whose origin has remained obscure.

A few examples have been shown in previous sections. Here, Figure 4.30 is again used to clarify the above explanation. The details of two interconnected nanoleaves (Figure 4.30(a)) indicate that the interface (marked by arrowheads) between the two leaves is fused together. In the HRTEM image (Figure 4.30(b)), the small NPs were able to join together to form a larger crystal under laser ablation in a liquid media. Different layers of NPs can be seen in Figure 4.30(b), presenting a dark colour contrast in the image. When structurally similar surfaces of particles approach, there will be a driving force to form chemical bonds between atoms and it is also possible that a number of NPs rest on top of the other crystals. However, typically, surfaces are not atomically flat. Coherence will then be achieved by distortion in some areas of the interface, and edge dislocations will form in the regions of step sites (Figure 4.30(c), arrowheads highlighted for clarity). The microdiffraction pattern (Figure 4.30(d)) from the edge of the nanoleaf in Figure 4.30(c) shows two sets of dot patterns, which almost overlap each other. This further confirms that slightly imperfect oriented attachment occurs between crystals of a single structure.

Imperfect attachment involves not just simple rotation of two particles. Figure 4.31 is a HRTEM image of a portion of a crystal formed by attachment of at least eight primary particles. It is seen that the lattice planes of the denoted particles are almost perfectly aligned. Moreover, apparently, the lattice planes go straight through the contact areas (see arrows for clarity), which the particles are epitaxially fused together. Bottlenecks between the adjacent particles are still visible (3rd and 4th particles). When seen at a low angle, one can even observe how the individual

particles are aligned like bricks in a wall (6th, 7th and 8th), where the second layer of bricks is just starting to be laid on top of the first (4th and 5th). This type of oriented attachment implies that the rods should occur when the NP supply within the solution becomes saturated in the later stage of growth. The width of the rods is almost identical to the diameter of the particles. As long as the surfaces of the attaching particles are dimensionally similar, the solution environment will allow the components to adjust their positions within an aggregate once it has formed.

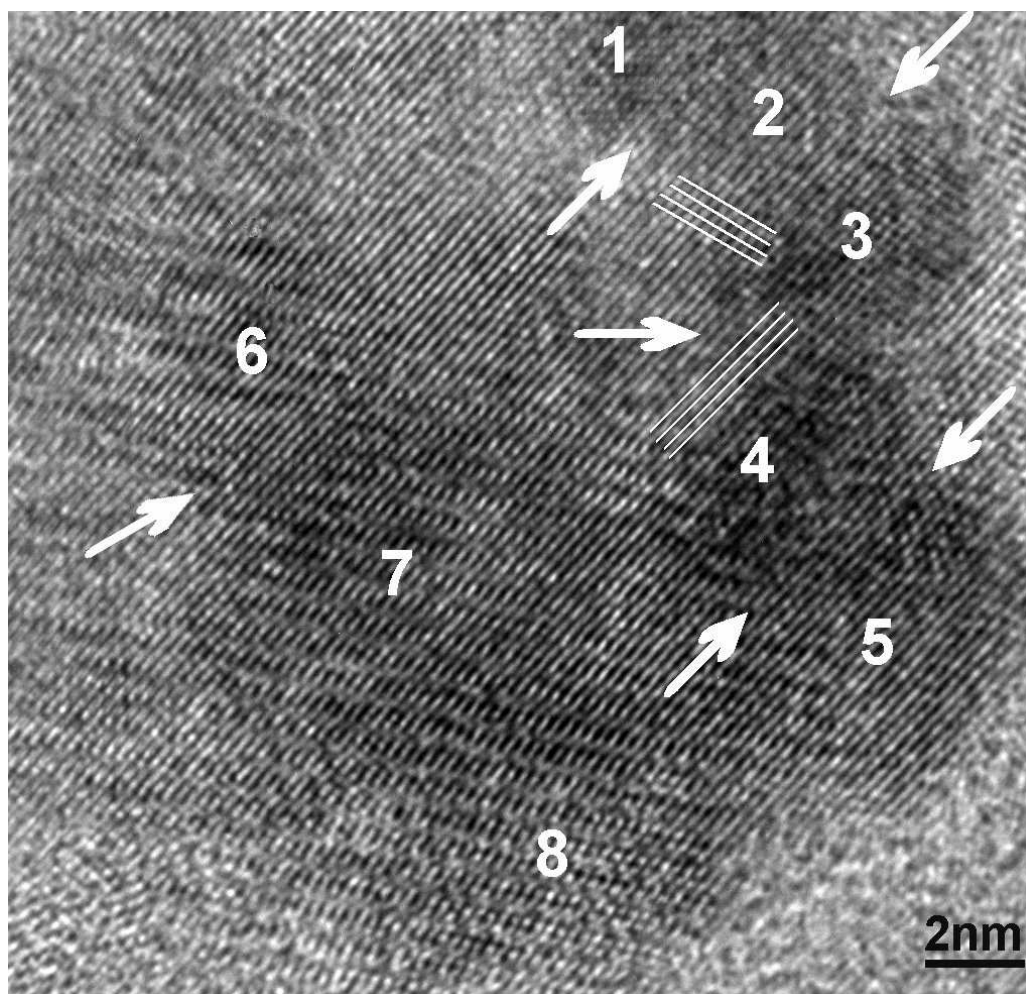


Figure 4.31 Representative lattice-resolved HRTEM image of carbon nitride crystalline aggregates (white arrows indicate the boundaries between the crystalline NPs, lines show the lattice planes within the crystallite.), the numbers denote the individual NP.

§ 4.4.2.3 Proposed model for self-organized growth

From emission spectra and simulations, it is known [124] that laser ablation of a graphite target in water using 70 mJ/pulse energy of laser produces pressures and temperature inside the plasma plume of ~1 GPa and 6000 K, respectively. At these extremely high pressures and temperatures, several chemical reactions and physical processes that are not possible at conventional conditions will take place among ablated species, solvent and surfactant molecules. These reactions induce the formation of particles in the solution.

In the light of previous results, a model for the sequential growth pathway of carbon nitride superstructures has been proposed, illustrated in Figure 4.32, involving structural and morphology modifications of carbon nitride. This complicated reaction process could generally be expressed in terms of following overall equation: $4\text{NH}_3 + 3\text{C} \rightarrow \text{C}_3\text{N}_4 + 6\text{H}_2$, which is consistent with the chemical mechanism proposed in a recent study by Yin *et al.* [34].

The model is as follows. The highly energetic C and N species in the ablation plume (Figure 4.32(a)) initially condense into small monodispersed spherical C_3N_4 nanoparticles (Figure 4.32(b)). Due to the very short laser pulse length (15 ns) and the fact that the plume is rapidly quenched by the surrounding liquid, the growth times of these nuclei are very short. This may aid the preferential formation of small metastable nuclei with a uniform particle distribution [125], as seen in Figure 4.11(a). With increasing concentration (caused by longer ablation times), the spherical C_3N_4 nuclei begin to join together to form short rods (Figure 4.32(c)) [126], which then elongate on exposure to more laser energy as a result of chemical reactions with the liquid phase [127]. When the concentration of the NRs becomes sufficiently high, they begin to line side-by-side, eventually forming multilayer leaf-like structures (Figure 4.32(d)). With increasing density of leaf-like structures in the suspension, the leaf-like structures themselves begin to aggregate into large connected networks (Figure 4.32(e)), which eventually rearrange to form mesoscale superstructures, such as spheres and finally flower-like structures (Figure 4.32(f)).

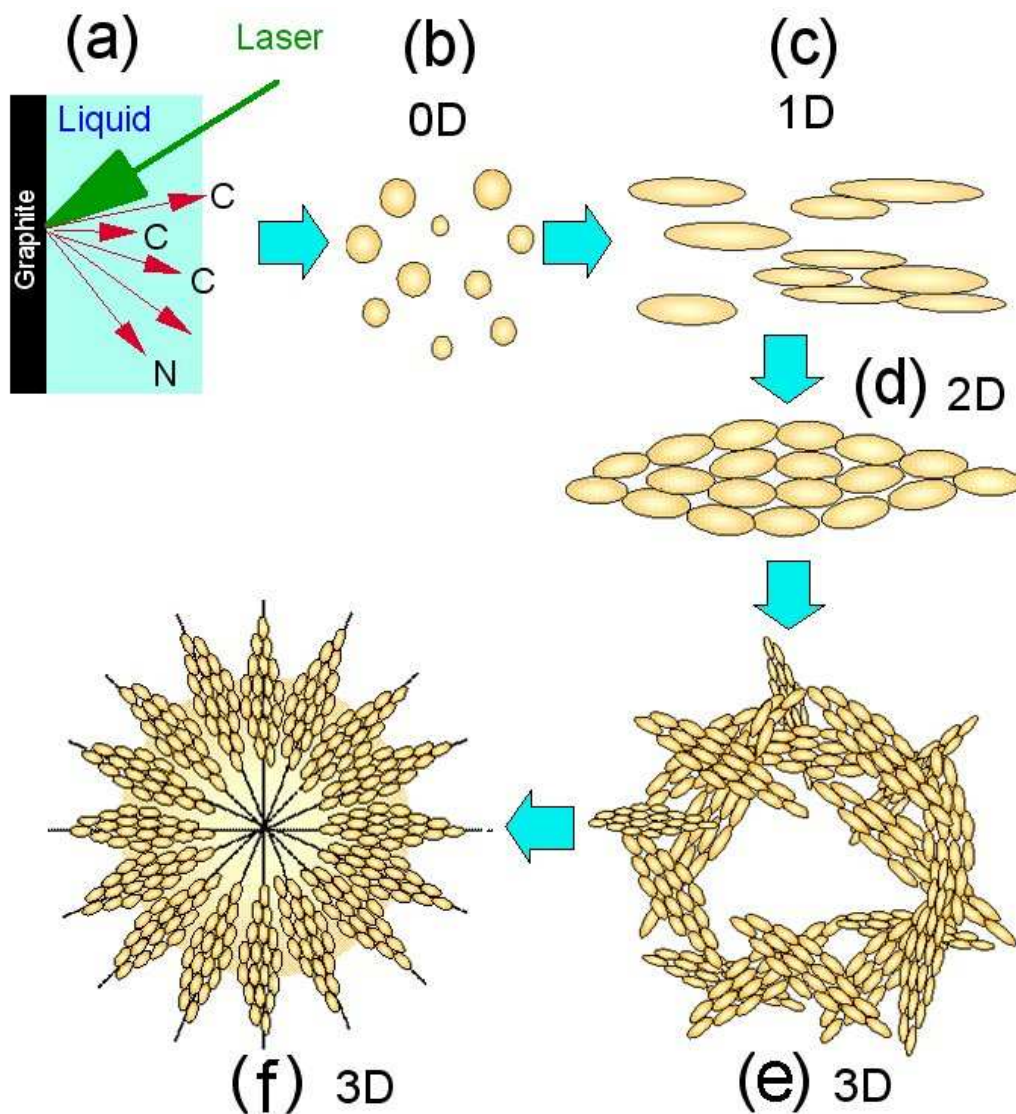


Figure 4.32 Proposed sequential growth pathway model involving structural and morphology modifications of carbon nitride, with increasing ablation time (and concentration) going from (a) to (f). (a) The ablation plume creates energetic C and N species. (b) The species condense into monodispersed spherical C_3N_4 0D nanoparticles. (c) Nanoparticles elongate into 1D rods, and these start to aggregate to form multilayer structures. (d) The multilayered structures increase in size until they form two-dimensional (2D) leaf-like structures of size 40 nm by ~ 200 nm. (e) The leaf-like structures aggregate into a network of three-dimensional (3D) joined clusters. (f) Clusters undergo a phase transformation to produce micron-scale ‘flowerlike’ particles with multi-fold symmetry.

§ 4.5 Conclusions

Fabrication of well-organized carbon nitride leaf-like nanostructures can be achieved by LP-PLA using solid graphite and ammonia solution, without the assistance of any surfactants or pretreatment. Evidence has been provided to illustrate that the nanostructured materials produced in this way are composed of crystalline α - or β - C_3N_4 . The morphology of the crystalline material changes at different length scales. The basic building blocks are 0D nanoparticles or 1D nanorods (10 nm by ~ 200 nm) which, given sufficient concentration, then aggregate to form larger, ordered leaf-like structures (30-50 nm by ~ 200 nm). Other geometrically complex C_3N_4 nanostructures such as interconnected networks, large mesoscale clusters, and multifold-symmetry flower-like structures can also be fabricated via a self-assembly ordered scheme. Factors such as the ammonia concentration, laser energy, and the reaction time are important in defining the structures observed. Longer ablation times increased the length of the nanoleaf but did not significantly increase the width above a maximum value of 80 ± 20 nm. In addition, with increasing ablation time more nitrogen becomes incorporated into the structures, which improves the crystallinity of the component NRs, but does not affect the crystallinity of the overall nanoleaf structures. High laser fluence and high concentration of ammonia solution also help to increase the ordering in the nanomaterials. The C_3N_4 nanostructures have a wide bandgap of ~ 4.0 eV, which can be tuned over a small range (3.90-4.05 eV) by varying the ablation time, suggesting potential applications for the development of semiconductor or optical devices.

With important discoveries continuing to be made in the field of nanomaterials, fulfilling the potential applications will require a greater control of material properties, along with a better understanding of the mechanisms for nanocrystal nucleation and growth. Attempts to understand the self-assembly processes of Group IV-V compounds, such as carbon nitride, are still in their infancy, and synthesis of complex nanostructures has only just begun. Our work indicates that the formation mechanism of highly ordered architectures appears to involve an increase of the structural complexity from 0D NPs to 1D NRs, and then broadening of these into 2D nanoleaves, which finally coalesce to 3D flowers. This unique process provides

more insight into laser-induced chemical reactions in general, and of crystalline carbon nitride phases in particular, and may provide an alternative synthesis method for other composite nanostructures. For example, we have also demonstrated that a novel hierarchical and self-similar growth process can happen in zinc oxide materials by LP-PLA of a zinc plate submerged in aqueous SDS solution [128]. The growth mechanism here also appears to involve an increase of the structural complexity from 0D NPs to 1D NRs, and then broadening of these into 2D ‘nano-leaf’ structures. Details can be seen in Chapter 6.

Further evidence for these findings may be obtained by using a technique such as electron energy loss spectroscopy (EELS) which would be able to distinguish between N-bonded-to-C (as in C_3N_4) or in another form. Future studies may also include the use of other nitrogen-containing liquids (such as hydrazine), which may facilitate the generation of nitrogen atoms and radicals more readily. Addition of surfactants into the solution may also influence the aggregation and dispersal of the nanomaterials. Similar synthesis routes for other Group IV-V crystalline compounds may also be possible using this ‘brute force’ LP-PLA approach, and appropriate target materials and liquids will be explored.

Bibliography

- [1] Liu A Y, Cohen M. L, *Science*, 1989, **245**, 841.
- [2] Wei J, Hing P, Mo Z Q, *Surf. Interface Anal.*, 1999, **28**, 208.
- [3] Teter D M, Hemley R J, *Science*, 1996, **271**, 53.
- [4] Yoon Y G, Pfrommer B G, Mauri F, Louie S G, *Phys. Rev. Lett.*, 1998, **80**, 3388.
- [5] Mattesini M, Matar S F, Etourneau J, *J. Mater. Chem.*, 2000, **10**, 709.
- [6] Mattesini M, Matar S F, Snis A, Etourneau J, Mavromaras A, *J. Mater. Chem.*, 1999, **9**, 3151.
- [7] Kouvetakis J, Bandari A, Todd M, Wilkens B, Cave N, *Chem. Mater.*, 1994, **6**, 1376.
- [8] Liu A Y, Wentzcovitch R M, *Phys. Rev. B*, 1994, **50**, 10362.
- [9] Marumo F, Syono, Y, *Acta Crystallogr.*, 1971, **B27**, 1868.
- [10] Veprek S, Weidmann J, Glatz F, *J. Vac. Sci. Technol. A*, 1995, **13**, 2914.
- [11] Matar S F, Mattesini M, *Chimie/Chemisty*, 2001, **4**, 255.
- [12] Malkow T, *Mat. Sci. Eng. A*, 2000, **292**, 112.
- [13] Guo Y, Goddard W A, *Chem. Phys. Lett.*, 1990, **237**, 72.
- [14] Guo Q X, Xie Y, Wang X J, Lv S C, Hou T, Liu X M, *Chem. Phys. Lett.*, 2003, **380**, 84.
- [15] Lu W, Komvopoulos K, *J. Appl. Phys.*, 1999, **85**, 2642.
- [16] Zhang Y, Zhou Z, Li H, *Appl. Phys. Lett.*, 1995, **68**, 634.
- [17] Fang P H, *Appl. Phys. Lett.*, 1996, **136**, 69.
- [18] Chen Y, Guo L P, Wang E G, *Philos. Mag. Lett.*, 1997, **75**, 155.
- [19] Yen T Y, Chou C P, *Solid State Commun.*, 1995, **95**, 281.
- [20] Hayashi Y, Krishna K M, Ebisu H, Soga T, Umeno M, Jimbo T, *Diamond. Rel. Mater.*, 2001, **10**, 1002.
- [21] Yu K M, Cohen M L, Haller E E, Hansen W L, Liu A Y, Wu I C, *Phys. Rev. B*, 1994, **49**, 5034.

- [22] Wu D W, Fu D J, Guo H X, Zhang Z H, Meng X Q, Fan X J, *Phys. Rev. B.*, 1997, **56**, 4949.
- [23] Lopez S, Dunlop H M, Benmalek M, Tourillon G, Wong M S, Sproul W D, *Surf. Interface Anal.*, 1997, **25**, 315.
- [24] Sjostrom H, Stafstrom S, Boman M, Sundgren J E, *Phys. Rev. Lett.*, 1995, **75**, 1336.
- [25] Méndez J M, Gaona-Couto A, Muhl S., Jiménez-Sandoval S, *J. Phys.: Condens. Matter*, 1999, **11**, 5225.
- [26] Marton D, Boyd K J, Al-Bayati A H, Todorov S S, Rabalais J W, *Phys. Rev. Lett.*, 1994, **73**, 118.
- [27] Boyd K J, Marton D, Todorov S S, Al-Bayati A H, Kulik J, Zuhr R A, Rabalais J W, *J. Vac. Sci. Technol. A*, 1995, **13**, 2110.
- [28] Alvarez F, Victoria N M, Hammer P, Freire F L, dos Santos M C, *Appl. Phys. Lett.*, 1998, **73**, 1065.
- [29] Chen L C, Lu T R, Kuo C T, Bhusari D M, Wu J J, Chen K H, Chen T M, *Appl. Phys. Lett.*, 1998, **72**, 3449.
- [30] Ren Z F, Huang Z P, Xu J W, Wang J H, Bush P, Siegal M P, Provencio P N, *Science*, 1998, **282**, 1105.
- [31] Ren Z M, Du Y C, Ying Z F, Qiu Y X, Xiong X X, Wu J D, Li F M, *Appl. Phys. Lett.*, 1994, **65**, 1361.
- [32] Montigaud H, Tanguy B, Demazeau G, Alves I, Birot M, Dunogues J, *Diamond. Relat. Mater.*, 1999, **8**, 1707.
- [33] Bai Y J, Lu B, Liu Z G, Li L, Cui D L, Xu X G, Wang Q L, *J. Cryst. Growth*, 2003, **247**, 505.
- [34] Yin L W, Bando Y, Li M S, Liu Y X, Qi Y X, *Adv. Matar.*, 2003, **15**, 1840.
- [35] Rodil S E, Milne W I, Robertson J, Brown L M, *Appl. Phys. Lett.*, 2000, **77**, 1458.
- [36] Xin H, Lin C, Xu W P, L. Wang, S Zou, X Wu, X Shi, H Zhu, *J. App. Phys.*, 1996, **79**, 2364.
- [37] Gouzman I, Brener R, Hoffman A, *Surf. Sci.*, 1995, **333**, 283.
- [38] Aoi Y, Ono K, Kamijo E, *J. Appl. Phys.*, 1999, **86**, 2318.

- [39] Matsumoto S, Xie E Q, Izumi F, *Diamond Relat. Mater.*, 1999, **8**, 1175.
- [40] Fang P H, *J. Mater. Sci. Lett.*, 1995, **14**, 536.
- [41] DeVries R C, *Mat. Res. Innovat.*, 1997, **1**, 161.
- [42] Riedel R, *Adv. Mater.*, 1994, **6**, 549.
- [43] Badding J V, *Adv. Mater.*, 1997, **9**, 877.
- [44] Stevens A J, Koga T, Agee C B, Aziz M J, Lieber C M, *J. Am. Chem. Soc.*, 1996, **118**, 10900.
- [45] Badding J V, Nesting D C, *Chem. Mater.*, 1996, **8**, 535.
- [46] Sharma A K, Ayyub P, Multani M S, Adhi K P, Ogale S B, Sunderaraman M, Upadhyay D D, Banerjee S, *Appl. Phys. Lett.*, 1996, **69**, 3489.
- [47] Wixom M R, *J. Am. Ceram. Soc.*, 1990, **73**, 1973.
- [48] May P W, Burrige P R, Rego C A, Tsang R S, Ashfold M N R, Rosser K N, Tanner R E, Cherns D, Vincent R, *Diamond Relat. Mater.*, 1996, **5**, 354.
- [49] He D W, Zhang F X, Zhang X Y, Qin Z C, Zhan M, Liu R P, Xu Y F, Wang W K, *J. Mater. Res.*, 1998, **13**, 3458.
- [50] Frauenheim T, Jungnickel G, Sitch P, Kaukonen M, Weich F, Widany J, Porezag D, *Diamond Relat. Mater.*, 1998, **7**, 348.
- [51] Korsounskii B L, Pepekina V I, *Russ. Chem. Rev.*, 1997, **66**, 901.
- [52] Lowther J E, *Phys. Rev. B*, 1999, **59**, 11683.
- [53] Dymont V P, Nekrashevich E M, Starchenko I M, *Solid State Commun.*, 1999, **111**, 443.
- [54] Benard D J, Linnen C, Harker A, Michels H H, Addison J B, Ondercin R, *J. Phys. Chem. B*, 1998, **102**, 6010.
- [55] N Tsubouchi, Y Horino, B Enders, A Chayahara, A Kinomura, K Fujii, *Appl. Phys. Lett.*, 1998, **72**, 1412.
- [56] D F Franceschini, F L Freire Jr., S R P Silva, *Appl. Phys. Lett.*, 1996, **68**, 2645.
- [57] A Snis, S F Matar, O Plashkevych, H Agren, *J. Chem. Phys.*, 1999, **111**, 9678.
- [58] He J L, Chang W L, *Surf. Coat. Technol.*, **99**, 1998, 184.
- [59] Hsu C Y, Hong F C -N, *Diamond Relat. Mater.*, 1999, **8**, 1315.
- [60] Tani Y, Aoi Y, Kamijo E, *Appl. Phys. Lett.*, 1998, **73**, 1652.

- [61] Chen G L, Li Y, Lin J, Huan C A, Guo Y P, *Diamond Relat. Mater.*, 1999, **8**, 1906.
- [62] Alves I, Demazeau G, Tanguy B, Weill F, *Solid State Commun.*, 1999, **109**, 697.
- [63] Johnson D J, Chen Y, He Y, Prince R H, *Diamond Relat. Mater.*, 1997, **6**, 1799.
- [64] Kouvetakis J, Bandari A, Todd M, Wilkens B, Cave N, *Chem. Mater.*, 1994, **6**, 811.
- [65] Lu T R, Kuo C T, Chen T M, *Thin Solid Films*, 1997, **308**, 126.
- [66] Song H W, Cui F Z, He X M, Li W Z, Li H D, *J. Phys.: Condens. Matter*, 1994, **6**, 6125.
- [67] Martin-Gil J, Martin-Gil F J, Sarikaya M, Qian M, José-Yacamán M, Rubio A, *J. Appl. Phys.*, 1997, **81**, 2555.
- [68] Kozlov M E, Hirabayashi M, Nozaki K, Tokumoto M, Ihara H, *Appl. Phys. Lett.*, 1995, **66**, 1199.
- [69] Vlodarchik E, Trebinski R, *Shock Waves*, 1997, **7**, 231.
- [70] Hirai H, Kondo K, Yoshizawa N, Shiraishi M, *Chem. Phys. Lett.*, 1994, **226**, 595.
- [71] Bousetta A, Lu M, Bensaoula A, Shultz A, *Appl. Phys. Lett.*, 1994, **65**, 696.
- [72] Hammer P, Victoria N M, Alvarez F, *J. Vac Sci Technol. A*, 2000, **18**, 2277.
- [73] Vinu A, Ariga K, Mori T, Nakanishi T, Hishita S, Golberg D, Bando Y, *Adv. Mater.*, 2005, **17**, 1648.
- [74] Zimmerman J L, Williams R, Khabashesku V N, Margrave J L, *Nano Lett.*, 2001, **1**, 731.
- [75] Liu A Y, Cohen M L, *Phys. Rev. B*, **1990**, **41**, 10727.
- [76] Wang J B, Lei J L, Wang R H, *Phys. Rev. B*, 1998, **58**, 11890.
- [77] Lábár J L, In: Frank L, Ciampor F (Eds.), *Proceedings of EUREM*, vol. III, July 2000, **12**, Brno, pp. I379-380.
- [78] Lu T R, Kuo C T, Yang J R, Chen L C, Chen K H, Chen T M, *Surf. Coat. Tech.*, 1999, **115**, 116.
- [79] Likhacheva A Y, Paukshtis E A, Seryotkin Y V, Shulgenko S G, *Phys. Chem. Miner.*, 2002, **29**, 617.

- [80] Tabbal M, Merel P, Moisa S, Chaker M, Ricard A, Moisan M, *Appl. Phys. Lett.*, 1996, **69**, 1698.
- [81] Angleraud B, Mubumbila N, Tessier P Y, Fernandez V, Turban G, *Diamond Relat. Mater.*, 2001, **10**, 1142.
- [82] Shi J R, Xu Y J, Zhang J, *Thin Solid Films*, 2005, **483**, 169.
- [83] Le Normand F, Hommet J, Szorenyi T, Fuchs C, Fogarassy E, *Phys. Rev. B*, 2001, **64**, 235416.
- [84] Ripalda J M, Montero I, Galan L, *Diamond. Relat. Mater.*, 1998, **7**, 402.
- [85] Ogata K, Chubaci J F D, Fujimoto F, *J. Appl. Phys.*, 1994, **76**, 3791.
- [86] Khabashesku V N, Zimmerman J L, Margrave J L, *Chem. Mater.*, 2000, **12**, 3264.
- [87] Yang L, May P W, Yin L, Brown R, Scott T B, *Chem. Mater.*, 2006, **18**, 5058.
- [88] Yang L, May P W, Yin L, Scott T B, Smith J A, Rosser K N, *Nanotechnology*, 2006, **17**, 5798.
- [89] Pacholski C, Kornowski A, Weller H, *Angew. Chem. Int. Ed.*, 2002, **41**, 1188.
- [90] Zeng H C, *J. Mater. Chem.*, 2006, **16**, 649.
- [91] Liu B, Zeng H C, *Small*, 2005, **1**, 566.
- [92] Guo Y, Goddard III W A, *Chem. Phys. Lett.*, 1995, **237**, 72.
- [93] Devaux D, Fabbro R, Tollier L, Bartnicki E, *J. Appl. Phys.*, 1993, **74**, 2268.
- [94] Liu B, Zeng H C, *J. Am. Chem. Soc.*, 2004, **126**, 16744.
- [95] Filik J, *Spectroscopy Europe*, 2005, **17**, 10.
- [96] Chowdhury A K M S, Cameron D C, Hashmi M S J, *Thin solid films*, 1998, **332** 62.
- [97] Rodil S E, Ferrari A C, Robertson J, Milne W I, *J. Appl. Phys.*, 2001, **89**, 5425.
- [98] Ferrari A C, Rodil S E, Robertson J, *Phys. Rev. B*, 2003, **67**, 155306.
- [99] Ferrari A C, Robertson J, *Phys. Rev. B*, 2000, **61**, 14095, and references therein.
- [100] Wang X C, Wu P, Li Z Q, Jiang E Y, Bai H L, *J. Phys. D*, 2004, **37**, 2127.
- [101] Chen C X, Chen W Z, Zhang Y F, *Physica E*, 2005, **28**, 121.
- [102] György E, Mihailescu I N, Baleva M, Abrashev M, Trifonova E P, Szekeres A, Perrone A, *Mater. Sci. Eng. B*, 2003, **97** 251.
- [103] Lee E H, Hembree D M, Rao G R, Mansur L K, *Phys. Rev. B*, 1993, **48** 15540.

- [104] Terrones M, Redlich P, Grobert N, Trasobares S, Hsu W K, Terrones H, Zhu Y Q, Hare J P, Reeves C L, Cheetham A K, Rühle M, Kroto H W, Walton D R M, *Adv. Mater.*, 1999, **11**, 655.
- [105] Doniach S, Sunjic M, *J. Phys. C*, 1970, **3**, 285.
- [106] Hellgren N, Johansson M P, Broitman E, Hultman L, Sundgren J –E, *Phys. Rev. B*, 1999, **59**, 5162.
- [107] Muhl S, Méndez J M, *Diamond Relat. Mater.*, 1999, **8**, 1809.
- [108] Hellgren N, Guo J, Sâthe C, Agui A, Nordgren J, Luo Y, Ågren H, Sundgren J E, *Appl. Phys. Lett.*, 2001, **79**, 4348.
- [109] Souto S, Pickholz M, doc Santos M C, Alvarez F, *Phys. Rev. B*, 1998, **57**, 2536.
- [110] Díaz J, Paoliceli G, Ferrer S, Comin F, *Phys. Rev. B*, 1996, **54**, 8064.
- [111] Beamson G, Briggs D, *High Resolution XPS of Organic Polymers*, 1992, John Wiley and Sons, Chichester, p.182.
- [112] Jin R C, Cao Y W, Mirkin C A, Kelly K L, Schatz G C, Zheng J G, *Science*, 2001, **294**, 1901.
- [113] Tauc J, *Amorphous and liquid semiconductors*, 1974, London and New York: Plenum, p.171.
- [114] Link S, El-Sayed M A, *J. Phys. Chem. B*, 1999, **103**, 4212.
- [115] Fuge G M, Ashfold M N R., Henley S J, *J. Appl. Phys.*, 2006, **99**, 014309.
- [116] Claeysens F, Ashfold M N R, Sofoulakis E, Ristoscu C G, Anglos D, Fotakis C, *J. Appl. Phys.*, 2002, **91**, 6162.
- [117] Wang J B, Yang G W, Zhang C Y, Zhong X L, Ren Z A, *Chem. Phys. Letts.*, 2003, **367**, 10.
- [118] Liu B, Zeng H C, *J. Am. Chem. Soc.*, 2005, **127**, 18262.
- [119] Nikoobakht B, Wang Z L, El-Sayed M A, *J. Phys. Chem. B*, 2000, **104**, 8635.
- [120] Kralchevsky P A, Nagayama K, *Langmuir*, 1994, **10**, 23.
- [121] Penn R L, Banfield J F, *Science*, 1998, **281**, 969.
- [122] Banfield J F, Hamers R J, *Geomicrobiology: interactions between microbes and minerals*, vol. 35 of Reviews in Mineralogy, Banfield J F and Nealson K H, Eds, 1997, Mineralogical Society of America, Washington DC, pp.86-122.
- [123] Alivisatos A P, *Ber. Bunsenges Phys. Chem.*, 1997, **101**, 1573.

- [124] Vanheusden K, Warren W L, Seager C H, Tallant D R, Voigt J A, Gnade B E, *J. Appl. Phys.*, 1996, **79**, 7983.
- [125] Yang G W, Wang J B, *Appl. Phys. A*, 2000, **71**, 343.
- [126] Liu B, Zeng H C, *J. Am. Chem. Soc.*, 2004, **126**, 8124.
- [127] Shaw S J, Schiffers W P, Gentry T P, Emmony D C, *J. Phys. D*, 1999, **32**, 1612.
- [128] Yang L, May P W, Yin L, Scott T B, *Nanotechnology*, 2007, **18**, 215602.